Difference Potentials Method for Models with Dynamic Boundary Conditions and Bulk-Surface Problems

Yekaterina Epshteyn · Qing Xia

Received: date / Accepted: date

Abstract In this work, we consider parabolic models with dynamic boundary conditions and parabolic bulk-surface problems in 3D. Such partial differential equations based models describe phenomena that happen both on the surface and in the bulk/domain. These problems may appear in many applications, ranging from cell dynamics in biology, to grain growth models in polycrystalline materials. Using Difference Potentials framework, we develop novel numerical algorithms for the approximation of the problems. The constructed algorithms efficiently and accurately handle the coupling of the models in the bulk and on the surface, approximate 3D irregular geometry in the bulk by the use of only Cartesian meshes, employ Fast Poisson Solvers, and utilize spectral approximation on the surface. Several numerical tests are given to illustrate the robustness of the developed numerical algorithms.

 $\label{lem:keywords} \textbf{Keywords} \ \ Dynamic \ boundary \ conditions \cdot Bulk-surface \ models \cdot Difference \ Potentials \ method \cdot Cartesian \ grids \cdot Irregular \ geometry \cdot Finite \ difference \cdot Spectral \ approximation \cdot Spherical \ harmonics$

Mathematics Subject Classification (2010) 65M06 · 65M12 · 65M70 · 35K10

1 Introduction

The parabolic models with dynamic boundary conditions and parabolic bulk-surface models can be found in a variety of applications in fluid dynamics, materials science and biological applications, see for example, [11,10,28,12,15,7,22,4,16,19,24,26,5]. In many of these problems, partial differential equations (PDE) based models are used to capture dynamic phenomena that occur on the surface of the domain and in the bulk/domain. For instance, cell polarizations can be modeled by the switches of Rho GTPases between the active forms on the membrane (surface) and inactive forms in the cytosol (bulk) [12]. Another example is the modeling of the receptor-ligand dynamics, [15], to name a few examples here.

Yekaterina Epshteyn

Department of Mathematics, The University of Utah, 155 S 1400 E Rm. 233, Salt Lake City, UT, 84112, USA E-mail: epshteyn@math.utah.edu

Oing Xia

Department of Mathematics, The University of Utah, 155 S 1400 E Rm. 233, Salt Lake City, UT, 84112, USA E-mail: xia@math.utah.edu

In the current literature, there are only few numerical methods developed for such problems, and most of the methods are finite-element-based. For instance, a novel finite element scheme is proposed and analyzed for 3D elliptic bulk-surface problems in [14], where polyhedral elements are constructed in the bulk region, and the piecewise polynomial boundary faces serve as the approximation of the surface. The method in [14] employs two finite-element spaces, one in the bulk, and one on the surface. See also the review paper [13] on the finite element methods for PDEs on curved surfaces and the references therein. Also, space and time discretizations of 2D heat equations with dynamic boundary conditions are studied in [21], in a weak formulation that fits into the standard variational framework of parabolic problems. A flexible unfitted finite element method (cut-FEM) is proposed for 3D elliptic bulk-surface problems in [6]. The developed cut-FEM utilizes the same finite element space defined on a structured background mesh to solve the PDEs in the bulk region and on the surface. Another space-time cut-FEM approach, with continuous linear elements in space and discontinuous piecewise linear elements in time, is designed for 2D parabolic bulk-surface problems on time-dependent domains in [20]. Furthermore, a hybrid finite-volume-finite-element method is developed for 3D bulk-surface models in [9]. The hybrid method employs a monotone nonlinear finite volume method in the bulk, and the trace finite element method [29,30] is used to solve equations on the reconstructed polygonal approximation of the surface.

In this work, we develop novel numerical algorithms for 3D models with dynamic boundary conditions and bulk-surface coupling, within the framework of Difference Potentials method (DPM). The constructed numerical schemes efficiently and accurately handle the coupling of the models in the bulk and on the surface, approximate 3D irregular geometry in the bulk by the use of only Cartesian grids, employ Fast Poisson Solvers, and apply spectral approximation on the surface.

The paper is organized as follows. In Section 2, we discuss the two distinct yet related model problems that are considered in the current work, the parabolic model with dynamic boundary condition and parabolic bulk-surface problem in 3D. Next, in Section 3, we develop numerical methods based on Difference Potentials for these problems, and give the main steps of the constructed numerical algorithms. Lastly, in Section 4, we present the extensive numerical results (convergence, 3D views of the solutions, etc.) that show the robustness of the developed algorithms.

2 The Model with Dynamic Boundary Condition and Bulk-Surface Problem

In this work, we consider the following two models in 3D:

Heat equation with dynamic boundary condition on the surface (see related examples in [34, 21]),

$$u_t - \Delta u = f, \quad (x, y, z, t) \in \Omega \times \mathbb{R}^+,$$
 (1)

$$u_t + u + n \cdot \nabla u = \Delta_{\Gamma} u + g, \quad (x, y, z, t) \in \Gamma \times \mathbb{R}^+,$$
 (2)

$$u(x, y, z, 0) = u_0(x, y, z), \quad (x, y, z) \in \Omega \cup \Gamma.$$
 (3)

The bulk-surface problem (see related examples in [20, 15]),

$$u_t - \Delta u = f, \quad (x, y, z, t) \in \Omega \times \mathbb{R}^+,$$
 (4)

$$-n \cdot \nabla u = h(u, v), \quad (x, y, z, t) \in \Gamma \times \mathbb{R}^+, \tag{5}$$

$$v_t - \Delta_{\Gamma} v = g + h(u, v), \quad (x, y, z, t) \in \Gamma \times \mathbb{R}^+,$$
 (6)

$$u(x, y, z, 0) = u_0(x, y, z), \quad (x, y, z) \in \Omega,$$
 (7)

$$v(x, y, z, 0) = v_0(x, y, z), \quad (x, y, z) \in \Gamma.$$
 (8)

In the above models, Γ is a smooth boundary/surface of a bounded domain/bulk $\Omega \subset \mathbb{R}^3$, Δ_{Γ} is the Laplace-Beltrami operator defined on Γ , n denotes the outward unit normal vector. The function h(u,v) is the coupling relation between the bulk and the surface, and g in (2) or (6) is the source function on the surface. The initial data for the model (1)-(2) is given by function $u_0(x,y,z)$, $(x,y,z) \in \Omega \cup \Gamma$ and the initial data in (4)-(6) are given by functions $u_0(x,y,z)$, $(x,y,z) \in \Omega$ and $v_0(x,y,z)$, $(x,y,z) \in \Gamma$.

3 Algorithms Based on DPM

The current work is a continuation of the recent work in [2,3,18,23]. For the time being, we will consider the model with dynamic boundary conditions and the bulk-surface problem in a spherical domain, but the proposed methods can be extended to domains with more general geometry in 3D (and the main ideas of the algorithms will stay the same, see Remark 5 below). We employ a finite-difference scheme for the underlying space discretization of the models in the bulk (1) or (4), combined with the idea of Difference Potentials Method (DPM) ([32] and very recent work [33,17,2,3,18], etc.) that provides flexibility to handle irregular domains and nontrivial boundary conditions (including, but not limited to, dynamic boundary conditions like (2), or surface equations like (6)) accurately and efficiently.

3.1 The Numerical Algorithm Based on DPM

Discretization in the Bulk:

Introduction of the Auxiliary Domain. As a first step of the numerical algorithm, we embed the original domain Ω into a computationally simple auxiliary domain $\Omega^0 \subset \mathbb{R}^3$, that we will select to be a cube in this work. Next, we introduce a Cartesian mesh to discretize the auxiliary domain Ω^0 , with mesh nodes $(x_j, y_k, z_l) = (x_0 + j\Delta x, y_0 + k\Delta y, z_0 + l\Delta z), (j, k, l = 0, 1, 2 ..., N)$. Here, (x_0, y_0, z_0) is the left-bottom corner point of the cubical auxiliary domain Ω^0 . For simplicity, we assume that the Cartesian mesh is uniform, i.e., $h := \Delta x = \Delta y = \Delta z$. To discretize the PDE (1) or (4) in the bulk, with a second order accuracy in space, we will consider the standard 7-point finite-difference stencil with a center placed at the point (x_j, y_k, z_l) :

$$\mathcal{N}_{j,k,l}^7 = \left\{ (x_j, y_k, z_l), (x_{j\pm 1}, y_k, z_l), (x_j, y_{k\pm 1}, z_l), (x_j, y_k, z_{l\pm 1}) \right\}. \tag{9}$$

Next, we define the important point sets that we will use as a part of the Difference Potentials framework (see Fig. 1):

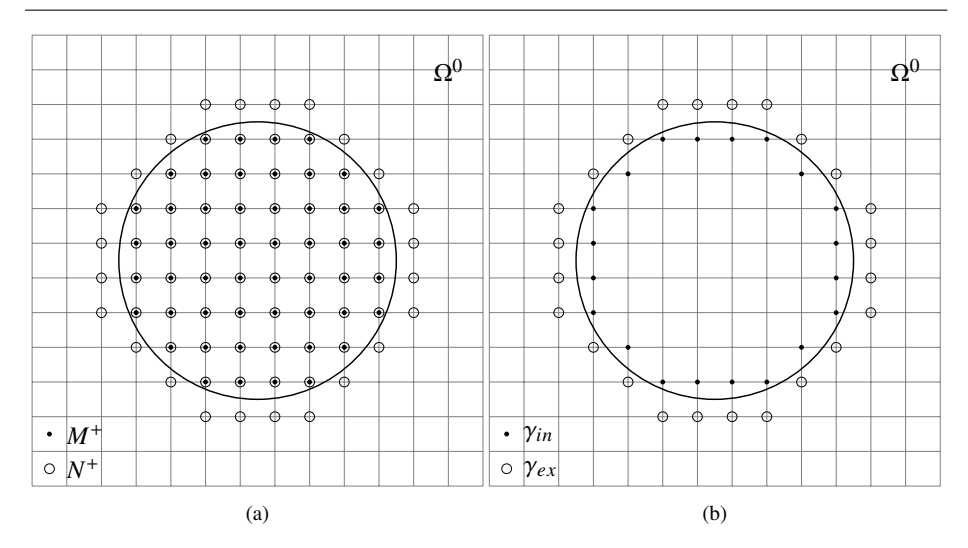


Fig. 1: Examples of point sets in the cross-sectional view: M^+ (solid dots) as a subset of N^+ (open circles), where solid dots in open circles show the overlap between M^+ and N^+ in the left figure; and the discrete grid boundary γ as the union of γ_{ex} (open circles) and γ_{in} (solid dots) in the right figure. The auxiliary domain is denoted as Ω^0 in both figures.

Definition 1 Introduce the following point sets:

- $M^0 = \{(x_j, y_k, z_l) \mid (x_j, y_k, z_l) \in \Omega^0\}$ denotes the set of all mesh nodes (x_j, y_k, z_l) that belong to the interior of the auxiliary domain Ω^0 ;
- $-M^+ = M^0 \cap \Omega = \{(x_j, y_k, z_l) \mid (x_j, y_k, z_l) \in \Omega\}$ denotes the set of all mesh nodes (x_j, y_k, z_l) that belong to the interior of the original domain Ω ;
- $M^-=M^0\backslash M^+=\{(x_j,y_k,z_l)\mid (x_j,y_k,z_l)\in\Omega^0\backslash\Omega\}$ is the set of all mesh nodes (x_j, y_k, z_l) that are inside of the auxiliary domain Ω^0 , but belong to the exterior of the original domain Ω ;
- $N^{+} = \left\{ \bigcup_{j,k,l} \mathcal{N}_{j,k,l}^{7} \mid (x_{j}, y_{k}, z_{l}) \in M^{+} \right\};$ $N^{-} = \left\{ \bigcup_{j,k,l} \mathcal{N}_{j,k,l}^{7} \mid (x_{j}, y_{k}, z_{l}) \in M^{-} \right\};$

 $-N^{0} = \left\{ \bigcup_{j,k,l} \mathcal{N}_{j,k,l}^{7} \mid (x_{j}, y_{k}, z_{l}) \in M^{0} \right\};$ The point sets N^{\pm} and N^{0} are the sets of all mesh nodes covered by the stencil $\mathcal{N}_{j,k,l}^{7}$ for every mesh node (x_i, y_k, z_l) in M^{\pm} and M^0 respectively;

- $-\gamma = N^+ \cap N^-$ defines a thin layer of mesh nodes that straddles the continuous boundary Γ and is called the discrete grid boundary;
- $-\gamma_{in} = M^+ \cap \gamma$ and $\gamma_{ex} = M^- \cap \gamma$ are subsets of the discrete grid boundary that lie inside and outside of the spherical domain Ω respectively.

Construction of the System of Discrete Equations for Models (1) and (4). In this work, we will use the trapezoidal time stepping (Crank-Nicolson scheme) to illustrate the approach based on Difference Potentials for the models with dynamic boundary conditions and for the bulk-surface problems. In general, any other stable time marching scheme can be employed in a similar way.

For the spatial discretization, we will employ the second-order finite-difference scheme using the 7-point stencil $\mathcal{N}_{i,k,l}^{7}$ as defined above. Assume now, that $u_{i,k,l}^{i}$ denotes a discrete solution computed at the time level t^i at the mesh node (x_j, y_k, z_l) . Then, the discrete system of equations for (1) and (4) obtained using trapezoidal time approximation combined with the second-order central finite-difference approximation in space is,

$$L_{h,\Delta t} u_{i,k,l}^{i+1} = F_{i,k,l}^{i+1}, \quad (x_j, y_k, z_l) \in M^+, \tag{10}$$

where, we introduced the discrete linear difference operator $L_{h,\Delta t} \equiv \Delta_h - \sigma I$ with $\sigma = 2/\Delta t$, Δ_h -the discrete Laplace operator defined on point set M^+ , I-the identity matrix of the same size as Δ_h , the right-hand side function $\hat{F}_{i,k,l}^{i+1} \equiv -(\Delta_h + \sigma I)u_{i,k,l}^i - \hat{f}_{i,k,l}^{i+1} - f_{i,k,l}^i$, and $u_{i,k,l}^{i+1} \approx u(x_j, y_k, z_l, t^{i+1}).$

The Discrete Auxiliary Problem (AP). One of the important steps of DPM-based methods is the introduction of the auxiliary problem (AP). The discrete APs play a key role in construction of the Particular Solution and the Difference Potentials operators as a part of DPM-based algorithm proposed in this work.

Definition 2 At time t^{i+1} , given the grid function q^{i+1} on M^0 , the following difference equations (11)–(12) are defined as the discrete Auxiliary Problem (AP):

$$L_{h,\Delta t} w_{j,k,l}^{i+1} = q_{j,k,l}^{i+1}, \quad (x_j, y_k, z_l) \in M^0,$$

$$w_{j,k,l}^{i+1} = 0, \quad (x_j, y_k, z_l) \in N^0 \backslash M^0.$$
(11)

$$w_{i,k,l}^{i+1} = 0, \quad (x_j, y_k, z_l) \in N^0 \backslash M^0.$$
 (12)

Here, the discrete linear operator $L_{h,\Delta t} = \Delta_h - \sigma I$ is the linear operator similar to the one introduced in (10), but is defined now on a larger point set M^0 .

Remark 1 The homogeneous Dirichlet boundary condition (12) in the AP is chosen merely for efficiency of our algorithm, i.e. we employ Fast Poisson Solvers to solve the APs. In general, other boundary conditions can be selected for the AP as long as the defined AP is well-posed and can be solved computationally efficiently.

Construction of the Particular Solution. Let us denote by $G_{h,\Delta t}F_{j,k,l}^{i+1}$, $(x_j,y_k,z_l)\in N^+$, the Particular Solution of the fully discrete problem (10). The Particular Solution is defined on N^+ at time level t^{i+1} , and is obtained by solving the AP (11)–(12) with the following right hand side:

$$q_{j,k,l}^{i+1} = \begin{cases} F_{j,k,l}^{i+1}, & (x_j, y_k, z_l) \in M^+, \\ 0, & (x_j, y_k, z_l) \in M^-, \end{cases}$$
 (13)

and by restricting the computed solution from N^0 to N^+ .

Construction of the Difference Potentials and Boundary Equations with Projections. To construct the Difference Potentials, let us first define a linear space W_{γ} of all grid functions $w_{\gamma}^{i+1}(x_j, y_k, z_l)$ at t^{i+1} on γ . The functions are extended by zero to other points in N^0 set. These grid functions w_{γ}^{i+1} are called densities on the discrete grid boundary γ at the time level t^{i+1} .

Definition 3 The *Difference Potential* associated with a given density $w_{\gamma}^{i+1} \in W_{\gamma}$ is the grid function $P_{N^+\gamma}w_{\gamma}^{i+1}$ defined on N^+ at the time level t^{i+1} , and is obtained by solving the AP (11)–(12) with the following right hand side:

$$q_{j,k,l}^{i+1} = \begin{cases} 0, & (x_j, y_k, z_l) \in M^+, \\ L_{h,\Delta t}[w_{\gamma}^{i+1}], & (x_j, y_k, z_l) \in M^-, \end{cases}$$
 (14)

and by restricting the solution from N^0 to N^+ .

Next, we will introduce the trace operator. Given a grid function w^{i+1} defined on the point set N^+ , we denote by $Tr_{\gamma}w^{i+1}$ the trace or restriction of w^{i+1} from N^+ to the discrete grid boundary γ . Similarly, we define $Tr_{\gamma_{in}}w^{i+1}$ as the trace or restriction of w^{i+1} from N^+ to $\gamma_{in} \subset \gamma$. We are ready to define an operator $P_{\gamma}: W_{\gamma} \to W_{\gamma}$ such that $P_{\gamma}w_{\gamma}^{i+1}:=Tr_{\gamma}P_{N^+\gamma}w_{\gamma}^{i+1}$. The operator P_{γ} is a projection operator. Now, we will state the key theorem for Difference Potentials Method, which allows us to reformulate the difference equation (10) defined on M^+ into equivalent *Boundary Equations with Projections* (BEP) defined on the discrete grid boundary γ only.

Theorem 1 (Boundary Equations with Projections (BEP)) At time t^{i+1} , the discrete density u_{γ}^{i+1} is the trace of some solution u^{i+1} on N^+ to the difference equation (10), i.e. $u_{\gamma}^{i+1} := Tr_{\gamma}u^{i+1}$, if and only if the following BEP holds:

$$u_{\nu}^{i+1} - P_{\gamma} u_{\nu}^{i+1} = G_{h,\Delta t} F_{\nu}^{i+1}, \quad (x_i, y_k, z_l) \in \gamma, \tag{15}$$

where $G_{h,\Delta t}F_{\gamma}^{i+1} := Tr_{\gamma}G_{h,\Delta t}F_{j,k,l}^{i+1}$ is the trace of the Particular Solution on the discrete grid boundary γ .

$$Proof See [32]$$
or $[18].$

Remark 2 Note, using that Difference Potential is a linear operator, we can recast (15) as

$$u_{m}^{i+1} - \sum_{n \in \gamma} A_{nm} u_{n}^{i+1} = G_{h,\Delta t} F_{m}^{i+1}, \quad m \in \gamma,$$
 (16)

where m is the index of a grid point in the set γ , and $G_{h,\Delta t}F_m^{i+1}$ is the value of the Particular Solution at the grid point with index m in the set γ .

Proposition 1 The rank of linear equations in BEP (15) is $|\gamma_{in}|$, which is the cardinality of the point set γ_{in} .

Proof The proof follows the lines of the proof in [32, 18], and we will present it below for reader's convenience. If the density $u_{\gamma_{ex}}^{i+1}$ on γ_{ex} to the difference equation (10) is given, then such discrete system will admit a unique solution $u_{j,k,l}^{i+1}$ defined on a set N^+ . Hence, the BEP (15) will have a unique solution, if $u_{\gamma_{ex}}^{i+1}$ is given. Thus, the solution u_{γ}^{i+1} to BEP (15) has dimension $|\gamma_{ex}|$, which is the cardinality of set γ_{ex} . As a consequence, the BEP (15) has rank $|\gamma| - |\gamma_{ex}| = |\gamma_{in}|$.

Next, we introduce the reduced BEP (17) defined only on γ_{in} that can be shown to be equivalent to the BEP (15) defined on γ .

Theorem 2 *The BEP* (15) *defined on* γ *in Theorem 1 is equivalent to the following BEP* (17) *defined on a smaller subset* $\gamma_{in} \subset \gamma$:

$$u_{\gamma_{in}}^{i+1} - Tr_{\gamma_{in}} P_{\gamma} u_{\gamma}^{i+1} = Tr_{\gamma_{in}} G_{h,\Delta t} F_{\gamma}^{i+1}, \quad (x_j, y_k, z_l) \in \gamma_{in}$$
 (17)

Moreover, the reduced BEP (17) contains only linearly independent equations.

Proof The proof follows the lines of the proof in [32,18] and we will present it below for reader's convenience. First, define the grid function:

$$\Phi^{i+1} := P^{i+1} + G^{i+1} - u_{\nu}^{i+1}, \quad \text{on } N^0, \tag{18}$$

where P^{i+1} is a solution to the AP (11)–(12) on N^0 with right hand side (14) using density u_{γ}^{i+1} , G^{i+1} is a solution to the AP (11)–(12) on N^0 with right hand side (13), and u_{γ}^{i+1} is extended from γ to N^0 by zero. By the construction of Φ^{i+1} , one can see that Φ^{i+1} is a solution to the following difference equation:

$$L_{h,\Delta t}[\Phi^{i+1}] = \begin{cases} F^{i+1} - L_{h,\Delta t}[u_{\gamma}^{i+1}], & \text{on } M^+, \\ 0, & \text{on } M^-. \end{cases}$$
 (19)

Therefore, we conclude that Φ^{i+1} solves the following homogeneous difference equations on the set M^- :

$$L_{h \wedge t} \Phi^{i+1} = 0, \quad \text{on } M^-. \tag{20}$$

Additionally, by construction of functions Φ^{i+1} , P^{i+1} and G^{i+1} , the grid function Φ^{i+1} satisfies the following boundary condition:

$$\Phi^{i+1} = 0, \quad \text{on } N^0 \backslash M^0. \tag{21}$$

Next, observe that the BEP (15) and the reduced BEP (17) can be reformulated using grid function Φ^{i+1} in (18) as follows:

$$\Phi^{i+1} = 0, \quad \text{on } \gamma, \quad (\text{BEP (15)}),$$
(22)

and

$$\Phi^{i+1} = 0, \quad \text{on } \gamma_{in}, \quad (\text{BEP (17)}).$$
(23)

Hence, it is enough to show that (22) is equivalent to (23) to prove the equivalence between the BEP (15) and the reduced BEP (17). First, note that if (22) is true, then (23) is obviously satisfied.

Now, assume that (23) is true and let us show that (22) holds. Consider problem (20): $L_{h,\Lambda t}\Phi^{i+1}=0$ on M^- , subject to boundary conditions (21) and (23), since the set γ_{in} $(N^0 \setminus M^0)$ is the boundary set for set M^- . Then we have the following discrete boundary value problem:

$$L_{h,\Delta t} \Phi^{i+1} = 0, \quad \text{on } M^-, \tag{24}$$

$$\Phi^{i+1} = 0, \quad \text{on } N^0 \backslash M^0, \tag{25}$$

$$\Phi^{i+1} = 0, \quad \text{on } N^0 \backslash M^0,$$

$$\Phi^{i+1} = 0, \quad \text{on } \gamma_{in},$$
(25)
$$\Phi^{i+1} = 0, \quad \text{on } \gamma_{in},$$
(26)

which admits a unique zero solution: $\Phi^{i+1} = 0$ on M^- . Since $\gamma_{ex} \subset M^-$, we conclude that $\Phi^{i+1} = 0$ on γ_{ex} , as well as on $\gamma \equiv \gamma_{ex} \cup \gamma_{in}$, which shows that (23) implies (22).

Thus, we showed that (22) is equivalent to (23), and therefore, BEP (15) is equivalent to the reduced BEP (17). Moreover, due to Proposition 1, the reduced BEP (17) consists of only linearly independent equations.

Similarly to (15)-(16), the reduced BEP (17) can be recast as

$$u_{m}^{i+1} - \sum_{\mathfrak{n} \in \gamma} A_{\mathfrak{n}m} u_{\mathfrak{n}}^{i+1} = G_{h,\Delta t} F_{m}^{i+1}, \quad m \in \gamma_{in}.$$
 (27)

Remark 3 The BEP (15) or (17) reduces degrees of freedom from $O(h^{-3})$ in the difference equation (10) to $O(h^{-2})$. In addition, the reduced BEP (17) defined on γ_{in} reduces the number of equations in BEP (15) by approximately one half, since $|\gamma_{in}| \approx |\gamma|/2$. Thus, using the reduced BEP (17) will further improve the computational cost in our numerical algorithm, especially in 3D, and we will use the reduced BEP as a part of the proposed numerical algorithm.

Additionally, let us note that the BEP (15) or the BEP (17) will admit multiple solutions since the system of equations (15) (and hence (17)) is equivalent to the system of difference equations (10) without imposed boundary conditions yet. Therefore, to construct a unique solution to BEP (17), we need to supply the BEP (17) with either the dynamic boundary condition (2), or the coupling conditions on the surface (5)-(6). To impose these conditions efficiently into BEP, we will introduce the extension operator (28) and combine (28) with the spectral approach discussed below for the approximation of the boundary conditions/surface equations.

Definition 4 The extension operator $\pi_{\gamma\Gamma}[u^{i+1}]$ of the function $u(x, y, z, t^{i+1})$ from a point $(x, y, z) \in \Gamma$ to $(x_j, y_k, z_l) \in \gamma$ is defined as:

$$\pi_{\gamma\Gamma}[u^{i+1}]|_{(x_j,y_k,z_l)} := u^{i+1}(x,y,z)|_{\Gamma} + \left. d\frac{\partial u^{i+1}(x,y,z)}{\partial n} \right|_{\Gamma} + \left. \frac{d^2}{2} \frac{\partial^2 u^{i+1}(x,y,z)}{\partial n^2} \right|_{\Gamma}, \tag{28}$$

where n is the unit outward normal vector on Γ , d is the signed distance between a point $(x_j, y_k, z_l) \in \gamma$ and the point of its orthogonal projection (x, y, z) on the continuous boundary Γ in the direction of n.

Basically, the extension operator (28) defines values of $\pi_{\gamma\Gamma}[u^{i+1}]$ at the point of the discrete grid boundary $(x_j, y_k, z_l) \in \gamma$ with the desired accuracy through the values of the continuous solution and its gradients at time t^{i+1} at the continuous boundary Γ of the domain. In particular, we consider the extension operator (28) defined in $(x_j, y_k, z_k) \in \gamma_{in}$ when we solve the reduced BEP (17). In addition, note that d and n need not to be known precisely, see Tables 2–5 in Section 4.3.

Discretization on the Surface:

Here, for simplicity, we assume that the surface Γ is a sphere with radius R. However, the proposed numerical algorithms can be extended to more general smooth domains and, hence, more general surfaces, and the main steps of the methods will stay the same (see Remark 5 below).

Case 1: Dynamic Boundary Conditions (2). We will use trapezoidal in time scheme for (2), but other time discretizations can be employed as well. Since, in this work Γ is a sphere, we have that the normal derivative satisfies,

$$\frac{\partial u(x,y,z,t)}{\partial n} = \frac{\partial u(x,y,z,t)}{\partial r}, \quad (x,y,z) \in \Gamma, \tag{29}$$

where n is the unit outward normal vector and r is the variable radius in the spherical coordinates, and similarly, $u_{nn} = u_{rr}$.

The discrete in time dynamic boundary condition (2) is

$$\frac{u^{i+1}(x, y, z) - u^{i}(x, y, z)}{\Delta t} = \frac{1}{2} \left(\Delta_{\Gamma} u^{i+1}(x, y, z) - u^{i+1}(x, y, z) - \frac{\partial u^{i+1}(x, y, z)}{\partial r} + g^{i+1}(x, y, z) + \Delta_{\Gamma} u^{i}(x, y, z) - u^{i}(x, y, z) - \frac{\partial u^{i}(x, y, z)}{\partial r} + g^{i}(x, y, z) \right),$$
(30)

for $(x, y, z) \in \Gamma$. Here, $u^{i+1}(x, y, z)$ is an approximation in time of $u(x, y, z, t^{i+1})$, and $g^{i+1}(x, y, z)$ is an approximation of $g(x, y, z, t^{i+1})$ at time level t^{i+1} . Also, note that, the Laplace-Beltrami operator on the sphere Γ with a radius R at time t^{i+1} can be obtained as,

$$\Delta_{\Gamma} u^{i+1}(x,y,z) = \frac{1}{R^2 \sin \theta} \frac{\partial}{\partial \theta} \left(\sin \theta \frac{\partial u^{i+1}(x,y,z)}{\partial \theta} \right) + \frac{1}{R^2 \sin^2 \theta} \frac{\partial^2 u^{i+1}(x,y,z)}{\partial \varphi^2}, \quad (31)$$

where (θ, φ) are the polar and azimuthal angles for a point $(x, y, z) \in \Gamma$. Next, from (30), we can express the term $u_r^{i+1}(x, y, z)$ as,

$$\frac{\partial u^{i+1}(x, y, z)}{\partial r} = \Delta_{\Gamma} u^{i+1}(x, y, z) - (1 + \sigma)u^{i+1}(x, y, z) + \sigma u^{i}(x, y, z) + g^{i+1}(x, y, z)
+ \Delta_{\Gamma} u^{i}(x, y, z) - u^{i}(x, y, z) - \frac{\partial u^{i}(x, y, z)}{\partial r} + g^{i}(x, y, z), \quad (x, y, z) \in \Gamma$$

$$= \Delta_{\Gamma} u^{i+1}(x, y, z) - (1 + \sigma)u^{i+1}(x, y, z)
+ \sigma u^{i}(x, y, z) + g^{i+1}(x, y, z) + u^{i}_{t}(x, y, z), \quad (x, y, z) \in \Gamma,$$
(32)

where $\sigma = 2/\Delta t$ as before, and $u_t^i(x, y, z)$ denotes the time derivative of u(x, y, z, t) at time level t^i ,

$$u_t^i(x,y,z) = \Delta_\Gamma u^i(x,y,z) - u^i(x,y,z) - \frac{\partial u^i(x,y,z)}{\partial r} + g^i(x,y,z). \tag{33}$$

We assume that $u_t^0(x, y, z)$ is known initially, since $u^0(x, y, z)$ and $g^0(x, y, z)$ are known at the initial time. Note, that the time derivative $u_t^{i+1}(x, y, z)$ at the next time level t^{i+1} , can be updated efficiently using the following formula (consequence of (2) and (30)),

$$u_t^{i+1}(x, y, z) = \sigma u^{i+1}(x, y, z) - \sigma u^i(x, y, z) - u_t^i(x, y, z), \quad (x, y, z) \in \Gamma,$$
 (34)

once we have computed $u^{i+1}(x, y, z)$ at time level t^{i+1} .

Furthermore, we note that $u_{rr}^{i+1}(x, y, z)$ can be expressed in terms of $u_r^{i+1}(x, y, z)$ if one subtracts (2) from (1) by extending (1) outside of domain Ω :

$$\frac{\partial^{2} u^{i+1}(x, y, z)}{\partial r^{2}} = -u^{i+1}(x, y, z) - \left(1 + \frac{2}{R}\right) \frac{\partial u^{i+1}(x, y, z)}{\partial r} - f^{i+1}(x, y, z) + g^{i+1}(x, y, z), \tag{35}$$

for $(x, y, z) \in \Gamma$. Also, note that the normal derivative $u_r^{i+1}(x, y, z)$ depends linearly on $u^{i+1}(x, y, z)$ as in (32), hence we only need to determine one unknown term $u^{i+1}(x, y, z)$ in the extension operator (28).

Spectral Approach. To combine extension operator (28) accurately and efficiently with dynamic boundary condition (30) (and, hence with (32)), we will introduce the spectral approximations at each time level t^{i+1} of the following two terms:

$$u^{i+1}(x, y, z) \approx \sum_{\kappa=1}^{L} a_{\kappa}^{i+1} \phi_{\kappa}(\theta, \varphi), \quad (x, y, z) \in \Gamma,$$
 (36)

where (θ, φ) are the polar and the azimuthal angles for a point $(x, y, z) \in \Gamma$.

Remark 4 Here, the number of spherical harmonics L does not depend on the underlying mesh sizes and depends on the properties of the solutions to the models.

Now, combining relations (32), (35) and (36) with the extension operator (28), we obtain

$$\pi_{\gamma\Gamma}[u^{i+1}]|_{(x_{j},y_{k},z_{l})} = u^{i+1}(x,y,z)|_{\Gamma} + d \frac{\partial u^{i+1}(x,y,z)}{\partial r} \Big|_{\Gamma} + \frac{d^{2}}{2} \frac{\partial^{2}u^{i+1}(x,y,z)}{\partial r^{2}} \Big|_{\Gamma}$$

$$= \left(1 - d(1+\sigma) + \frac{d^{2}}{2} \left(\left(\frac{2}{R} + 1\right)(1+\sigma) - 1\right)\right) u^{i+1}(x,y,z)$$

$$+ \left(d - \frac{d^{2}}{2} \left(\frac{2}{R} + 1\right)\right) \Delta_{\Gamma}u^{i+1}(x,y,z)$$

$$+ d(\sigma u^{i}(x,y,z) + g^{i+1}(x,y,z) + u^{i}_{t}(x,y,z))$$

$$- \frac{d^{2}}{2} \left(\left(\frac{2}{R} + 1\right)(\sigma u^{i}(x,y,z) + g^{i+1}(x,y,z) + u^{i}_{t}(x,y,z))\right)$$

$$+ \frac{d^{2}}{2} \left(-f^{i+1}(x,y,z) + g^{i+1}(x,y,z)\right)$$

$$\approx u^{i+1}_{\gamma}(x_{j},y_{k},z_{l})$$

$$= Aa^{i+1} + c^{i+1}, \quad (x_{j},y_{k},z_{l}) \in \gamma \text{ and } (x,y,z) \in \Gamma,$$

$$(37)$$

where a^{i+1} is the vector of the unknown spectral coefficients a_{κ}^{i+1} , c^{i+1} denotes the known vector:

$$\begin{split} c^{i+1} = &d(\sigma u^i(x,y,z) + g^{i+1}(x,y,z) + u^i_t(x,y,z)) \\ &- \frac{d^2}{2}((\frac{2}{R} + 1)(\sigma u^i(x,y,z) + g^{i+1}(x,y,z) + u^i_t(x,y,z))) \\ &+ \frac{d^2}{2}(-f^{i+1}(x,y,z) + g^{i+1}(x,y,z)), \end{split} \tag{41}$$

and d is the signed distance from the point (x_j, y_k, z_l) in γ to its foot point (x, y, z) on the continuous boundary Γ . The coefficient matrix A is assembled using the basis functions, i.e.,

$$A_{m,\kappa} = \left(1 - d_m(1+\sigma) + \frac{d_m^2}{2} \left(\left(\frac{2}{R} + 1\right) (1+\sigma) - 1 \right) \right) \phi_{\kappa}(\theta_m, \varphi_m) + \left(d_m - \frac{d_m^2}{2} \left(\frac{2}{R} + 1\right) \right) \Delta_{\Gamma} \phi_{\kappa}(\theta_m, \varphi_m)$$

$$(42)$$

where m is the index that represents a point in γ , (θ_m, φ_m) are the polar and azimuthal angles for the foot point $(x, y, z) \in \Gamma$ of a point m in γ , and d_m is the signed distance for this point. Note, A is assembled using whole point set γ . However, only the rows corresponding to γ_{in} will be used in our algorithm when we solve the reduced BEP (17).

Remark 5 a) In the special case of a sphere, the surface laplacian of a spherical harmonic is conveniently obtained by the following eigenvalue-eigenfunction relation:

$$\Delta_{\Gamma} Y_{\ell}^{\text{in}}(\theta, \varphi) = -\ell(\ell+1) R^2 Y_{\ell}^{\text{in}}(\theta, \varphi) \tag{43}$$

where $Y_\ell^{\mathrm{m}}(\theta,\varphi)$ is the spherical harmonic function of degree ℓ and order m (see detailed formulas (83)–(84) in Section 4.1) and R is the radius of the sphere, see also [27,31]. Another equivalent approach is to use (31) and (36), where the derivatives of the spherical harmonics $\frac{\partial \phi_k^{i+1}}{\partial \theta}$, $\frac{\partial^2 \phi_k^{i+1}}{\partial \theta^2}$, $\frac{\partial^2 \phi_k^{i+1}}{\partial \varphi^2}$ can be obtained using recursive formula [1]. In the numerical section, we adopt the relation (43) for the efficiency of the codes.

b) In this work, we showcase the versatility of the DPM framework for dynamic BC and bulk-surface problems, and we illustrate the ideas of the method using spherical geometry in 3D. We should note that, the basis functions in the spectral approximation of the terms in the extension operator in the DPM framework are not limited to spherical harmonics. For example, in the case of smooth geometry other than spheres, local radial basis functions can be employed instead of spherical harmonics. In addition, DPM-based algorithms were developed for models on domains with corners (2D) [25] or wedges (3D) [18]. Furthermore, one possible future direction is to replace the spectral approximation on the surface with a more general method that can handle arbitrary geometry, for instance using ideas of the trace finite element method (trace-FEM) [8,9] that utilizes the restriction (trace) of a volumetric finite element space of piecewise continuous trilinear functions, to solve surface equations. In addition, the choice of the discretization of the bulk equation in the DPM framework has also a flexibility (and can be selected to be FEM, for example).

Case 2: Bulk-Surface Coupling (5)-(6). As for the bulk-surface problems, we assume here that the surface Γ is also a sphere with radius R, and thus, the Laplace-Beltrami operator Δ_{Γ} at time t^{i+1} is computed using the eigenvalue approach (43). Again, the first order normal derivative is computed as $u_n(x, y, z, t) \equiv \nabla u(x, y, z, t) \cdot n = u_r(x, y, z, t)$ for $(x, y, z) \in \Gamma$.

To discretize in time equation on the surface (6), we will use trapezoidal in time scheme as it is used in the bulk (10). The discrete in time surface equation is (as a result of (6)):

$$\frac{v^{i+1}(x,y,z) - v^{i}(x,y,z)}{\Delta t} = \frac{1}{2} (\Delta_{\Gamma} v^{i+1}(x,y,z) + g^{i+1}(x,y,z) + h(u^{i+1}(x,y,z), v^{i+1}(x,y,z)) + v_{t}^{i}(x,y,z), \quad (x,y,z) \in \Gamma,$$

$$(44)$$

where $v_t^i = \Delta_{\Gamma} v^i + g^i + h(u^i, v^i)$. Note that, to compute the term v_t^i efficiently, we use the formula,

$$v_t^i(x, y, z) = \sigma v^i(x, y, z) - \sigma v^{i-1}(x, y, z) - v_t^{i-1}(x, y, z), \quad (x, y, z) \in \Gamma,$$
(45)

which is consequence of the discretization (44) and (6). Moreover, since from (5), we have that $h(u^{i+1}, v^{i+1}) = -u_r^{i+1}$, we obtain the following expression for u_r^{i+1} ,

$$\frac{\partial u^{i+1}(x, y, z)}{\partial r} = -\sigma v^{i+1}(x, y, z) + \Delta_{\Gamma} v^{i+1}(x, y, z)
+ \sigma v^{i}(x, y, z) + g^{i+1}(x, y, z) + v^{i}_{t}(x, y, z), \quad (x, y, z) \in \Gamma,$$
(46)

where as before, $\sigma = 2/\Delta t$.

a) Linear Bulk-Surface Coupling. For simplicity, we first consider case of linear coupling function h(u, v) in (5) similar to, for example, [6] and [14],

$$h(u, v) = u - v$$
, on Γ . (47)

Since $h(u^{i+1}, v^{i+1}) = u^{i+1} - v^{i+1}$ at time level t^{i+1} , and using equation (44), we have that,

$$u^{i+1}(x, y, z) = (1 + \sigma)v^{i+1}(x, y, z) - \Delta_{\Gamma}v^{i+1}(x, y, z) - \sigma v^{i}(x, y, z) - g^{i+1}(x, y, z) - v_{t}^{i}(x, y, z), \quad (x, y, z) \in \Gamma.$$
(48)

Spectral Approach. Similarly to model with dynamic boundary conditions, to couple accurately and efficiently discretization of the bulk equations, hence, the reduced BEP (17) with the discretization of the surface equation (6) combined with coupling function (47), we will employ idea of extension operator (28) together with the spectral approximation of the functions $v^{i+1}(x, y, z)$ and $\frac{\partial^2 u^{i+1}(x, y, z)}{\partial r^2}$, $(x, y, z) \in \Gamma$ at each time level t^{i+1} . Hence, for the density u_y^{i+1} , we combine the extension operator (28) together with

relations (46)-(48), to obtain:

$$\pi_{\gamma\Gamma}[u^{i+1}]|_{(x_j, y_k, z_l)} = u^{i+1}(x, y, z) + d\frac{\partial u^{i+1}(x, y, z)}{\partial r} + \frac{d^2}{2} \frac{\partial^2 u^{i+1}(x, y, z)}{\partial r^2}$$

$$= [(1 + \sigma)v^{i+1} - \Delta_{\Gamma}v^{i+1}] + d\left[-\sigma v^{i+1} + \Delta_{\Gamma}v^{i+1}\right] + \frac{d^2}{2} \frac{\partial^2 u^{i+1}}{\partial r^2}$$

$$+ \left[-\sigma v^i - g^{i+1} - v_t^i\right] + d\left[\sigma v^i + g^{i+1} + v_t^i\right],$$
(50)

where $(x, y, z) \in \Gamma$ is the foot point of a point (x_i, y_k, z_l) in the discrete grid boundary γ , and d is the signed distance from a point (x_i, y_k, z_l) in γ to its foot point $(x, y, z) \in \Gamma$.

Next, similarly to the approximation of the dynamic boundary conditions, to construct density u_{ν}^{i+1} efficiently for the bulk model (4), we assume spectral approximations of the terms $v^{i+1}(x, y, z)$ and, also of the term $\frac{\partial^2 u^{i+1}(x, y, z)}{\partial r^2}$ in the extension operator (50), i.e.,

$$v^{i+1}(x, y, z) \approx \sum_{\kappa=1}^{L} a_{\kappa}^{i+1} \phi_{\kappa}(\theta, \varphi), \quad (x, y, z) \in \Gamma,$$
 (51)

$$\frac{\partial^2 u^{i+1}(x,y,z)}{\partial r^2} \approx \sum_{\kappa=1}^L b_{\kappa}^{i+1} \phi_{\kappa}(\theta,\varphi), \quad (x,y,z) \in \Gamma,$$
 (52)

where θ and φ are the polar and the azimuthal angles of the point $(x, y, z) \in \Gamma$. Then, after we replace v^{i+1} and $\frac{\partial^2 u^{i+1}(x,y,z)}{\partial r^2}$ in (50) using the spectral approximations above, the approximation to the extension operator (50) is given by,

$$\pi_{\gamma\Gamma}[u^{i+1}]|_{(x_i,y_k,z_l)} \approx u_{\gamma}^{i+1} = Aa^{i+1} + Bb^{i+1} + c^{i+1}, \tag{53}$$

where a^{i+1} , b^{i+1} are the vectors that store the unknown spectral coefficients, and c^{i+1} denotes the known term:

$$c^{i+1} = \left[-\sigma v^{i}(x, y, z) - g^{i+1}(x, y, z) - v_{t}^{i}(x, y, z) \right]$$

+ $d \left[\sigma v^{i}(x, y, z) + g^{i+1}(x, y, z) + v_{t}^{i}(x, y, z) \right], \quad (x, y, z) \in \Gamma.$ (54)

The coefficient matrices A and B are computed as,

$$A_{m,\kappa} = (1 + \sigma)\phi_{\kappa}(\theta_{m}, \varphi_{m}) - \Delta_{\Gamma}\phi_{\kappa}(\theta_{m}, \varphi_{m}) + d_{m} \left[-\sigma\phi_{\kappa}(\theta_{m}, \varphi_{m}) + \Delta_{\Gamma}\phi_{\kappa}(\theta_{m}, \varphi_{m}) \right], \tag{55}$$

$$B_{m,\kappa} = \frac{d_m^2}{2} \phi_{\kappa}(\theta_m, \varphi_m). \tag{56}$$

Here m is the index that represents a point in γ , (θ_m, φ_m) are the polar and azimuthal angles for the foot point $(x, y, z) \in \Gamma$ of a point m in γ , and d_m is the signed distance for this point. Similarly, matrices A and B are assembled using the whole point set γ , but only the rows corresponding to the γ_{in} set will be used in our algorithm to solve the reduced BEP (17).

b) *Nonlinear Bulk-Surface Coupling*. Here, we consider the example of nonlinear coupling function h(u, v) in (5), similar to, for example, [15],

$$h(u, v) = uv. (57)$$

And, as before, at time level t^{i+1} , we will have $u^{i+1}v^{i+1} = -u_r^{i+1}$.

Spectral Approach. Similar to model with linear bulk-surface coupling (47), to couple accurately and efficiently discretization of the bulk equations, hence, the reduced BEP (17) with the discretization of the surface equation (6), we will employ idea of extension operator (28) together with the spectral approximation of the functions $v^{i+1}(x, y, z)$, $u^{i+1}(x, y, z)$ and $\frac{\partial^2 u^{i+1}(x,y,z)}{\partial r^2}$, $(x,y,z) \in \Gamma$ at the time level t^{i+1} , i.e.,

$$v^{i+1}(x, y, z) \approx \sum_{\kappa=1}^{L} a_{\kappa}^{i+1} \phi_{\kappa}(\theta, \varphi), \quad (x, y, z) \in \Gamma,$$
 (58)

$$u^{i+1}(x, y, z) \approx \sum_{\kappa=1}^{L} c_{\kappa}^{i+1} \phi_{\kappa}(\theta, \varphi), \quad (x, y, z) \in \Gamma,$$
 (59)

$$\frac{\partial^2 u^{i+1}(x,y,z)}{\partial r^2} \approx \sum_{\kappa=1}^L b_{\kappa}^{i+1} \phi_{\kappa}(\theta,\varphi), \quad (x,y,z) \in \Gamma, \tag{60}$$

where, as before, (θ, φ) are the polar and the azimuthal angles of the point $(x, y, z) \in \Gamma$. Then, the extension operator (28) becomes,

$$\pi_{\gamma\Gamma}[u^{i+1}]|_{(x_j,y_k,z_l)} = u^{i+1}(x,y,z) + d\frac{\partial u^{i+1}(x,y,z)}{\partial r} + \frac{d^2}{2}\frac{\partial^2 u^{i+1}(x,y,z)}{\partial r^2} \tag{61}$$

$$= u^{i+1} + d \left(-\sigma v^{i+1} + \Delta_{\Gamma} v^{i+1} + \sigma v^{i} + g^{i+1} + v^{i}_{t} \right) + \frac{d^{2}}{2} \frac{\partial^{2} u^{i+1}}{\partial r^{2}} \tag{62}$$

$$= u^{i+1} + d\left(-\sigma v^{i+1} + \Delta_{\Gamma} v^{i+1}\right) + \frac{d^2}{2} \frac{\partial^2 u^{i+1}}{\partial r^2} + d(\sigma v^i + g^{i+1} + v_t^i) \quad (63)$$

$$\approx u_{\gamma}^{i+1}(x_j, y_k, z_l)$$

$$= Aa^{i+1} + Bb^{i+1} + Cc^{i+1} + d^{i+1}, (x_i, y_k, z_l) \in \gamma \text{ and } (x, y, z) \in \Gamma, \quad (64)$$

where the coefficient matrices A, B, C for the unknown spectral coefficients $a^{i+1}, b^{i+1}, c^{i+1}$ are computed as,

$$A_{m,\kappa} = d_m \left[-\sigma \phi_{\kappa}(\theta_m, \varphi_m) + \Delta_{\Gamma} \phi_{\kappa}(\theta_m, \varphi_m) \right], \tag{65}$$

$$B_{m,\kappa} = \frac{d_m^2}{2} \phi_{\kappa}(\theta_m, \varphi_m),\tag{66}$$

$$C_{m,\kappa} = \phi_{\kappa}(\theta_m, \varphi_m). \tag{67}$$

Here, m is the index that represents a point in γ , (θ_m, φ_m) are the polar and azimuthal angles for the foot point $(x, y, z) \in \Gamma$ of a point m in γ , and d_m is the signed distance for this point. The vector d^{i+1} in (64) represents the known quantity,

$$d^{i+1} = d(\sigma v^i(x, y, z) + g^{i+1}(x, y, z) + v_t^i(x, y, z)), \quad (x, y, z) \in \Gamma,$$
(68)

and is computed at the same foot point $(x, y, z) \in \Gamma$ of a point m in γ . Again, matrices A, B and C are assembled for the entire point set γ , but only the rows corresponding to the γ_{in} set will be used to solve the reduced BEP (17).

Linearization of the nonlinear coupling (57). To efficiently combine the coupling equation (57) with the BEP (17) and with the discretization of the surface equation (44), we will consider linearization of (57) at time level t^{i+1} .

To linearize, we replace $v^{i+1}(x, y, z)$ in (57) at the time level t^{i+1} by the following approximation in time

$$v^{i+1}(x, y, z) = v^{i}(x, y, z) + \Delta t v_{t}^{i}(x, y, z) + O(\Delta t^{2})$$
(69)

where $\Delta t = O(h)$. Then, the linearization of (57) gives us,

$$-n \cdot \nabla u^{i+1}(x, y, z) \approx u^{i+1}(x, y, z)(v^{i}(x, y, z) + \Delta t v_{t}^{i}(x, y, z)), \quad (x, y, z) \in \Gamma,$$
 (70)

where v_t^i term is computed via the relation (45). Note, that using (46) together with spectral approximation in (58)-(59), we can formulate coupling relation (57) at t^{i+1} as,

$$\Rightarrow -(-\sigma v^{i+1}(x,y,z)+\Delta_\Gamma v^{i+1}(x,y,z)+\sigma v^i(x,y,z)+g^{i+1}(x,y,z)+v^i_t(x,y,z))$$

$$= u^{i+1}(x, y, z)(v^{i}(x, y, z) + \Delta t v_{t}^{i}(x, y, z)),$$
 (71)

$$\Rightarrow A'a^{i+1} - \sigma v^i(x, y, z) - g^{i+1}(x, y, z) - v_t^i(x, y, z) = C'c^{i+1},$$
 (72)

$$\Rightarrow -A'a^{i+1} + C'c^{i+1} = -\sigma v^i(x, y, z) - g^{i+1}(x, y, z) - v_t^i(x, y, z). \tag{73}$$

The expression (73) gives the linear relation between unknown spectral coefficients a_{κ}^{i+1} and c_{κ}^{i+1} . Here, the matrices A' and C' are defined as,

$$A'_{m,\kappa} = -(-\sigma\phi_{\kappa}(\theta_m, \varphi_m) + \Delta_{\Gamma}\phi_{\kappa}(\theta_m, \varphi_m)), \tag{74}$$

$$C'_{m,r} = \phi_{\kappa}(\theta_m, \varphi_m)(v^i + \Delta t v_t^i). \tag{75}$$

Here, (θ_m, φ_m) corresponds to the angles of the foot point $(x, y, z) \in \Gamma$ of a point m in γ_{in} (since we employ the reduced BEP), and $v^i + \Delta t v_t^i$ is the corresponding value for the same foot point m.

Remark 6 One possible improvement is to approximate v^{i+1} in (57) at t^{i+1} using the following higher order in time approximation:

$$v^{i+1}(x, y, z) \approx v^{i}(x, y, z) + \Delta t v_{t}^{i}(x, y, z) + \frac{\Delta t^{2}}{2} v_{tt}^{i}(x, y, z), \quad (x, y, z) \in \Gamma,$$
 (76)

where $v_{tt}^{i}(x,y,z)$ can be approximated using the finite difference approximation in time.

Reconstruction of the Solutions at time t^{i+1} :

Case 1: Dynamic Boundary Conditions. Next, we use the reduced BEP (17) combined with the approximation of the extension operator in the form (40), to obtain the least squares (LS) system of dimension $|\gamma_{in}| \times L$ for the unknown spectral coefficients a^{i+1} ,

$$[A - P_{\gamma}A]a^{i+1} = G_{h,\Delta t}F_{\gamma}^{i+1} - (c^{i+1} - P_{\gamma}c^{i+1}), \text{ on } \gamma_{in}.$$
 (77)

After that, we solve for the unknown spectral coefficients a^{i+1} , using the normal equation of the reformulated BEP (77).

Case 2: a) Linear Bulk-Surface Coupling. Similarly to the model with dynamic boundary conditions, we combine the reduced BEP (17) and the approximation of the extension operator in the form (53), to obtain the LS system of dimension $|\gamma_{in}| \times (2L)$ for the unknown spectral coefficients a^{i+1} and b^{i+1} .

$$[A - P_{\gamma}A]a^{i+1} + [B - P_{\gamma}B]b^{i+1} = G_{h,\Delta t}F_{\gamma}^{i+1} - (c^{i+1} - P_{\gamma}c^{i+1}), \text{ on } \gamma_{in}.$$
 (78)

Again, we solve for the unknown spectral coefficients a^{i+1} and b^{i+1} using the normal equation of the reformulated BEP (78).

Case 2: b) Nonlinear Bulk-Surface Coupling. Similarly to the model with dynamic boundary conditions and bulk-surface model with linear coupling, we combine the reduced BEP (17), the approximation to the extension operator in the form (64) and the coupling condition (73), to obtain the LS system of dimension $2|\gamma_{in}| \times (3L)$ for the unknown spectral coefficients a^{i+1} , b^{i+1} and c^{i+1} ,

$$[A - P_{\gamma}A]a^{i+1} + [B - P_{\gamma}B]b^{i+1} + [C - P_{\gamma}C]c^{i+1} = G_{h,\Delta t}F_{\gamma}^{i+1} - (d^{i+1} - P_{\gamma}d^{i+1}), \text{ on } \gamma_{in},$$
(79)

$$-A'a^{i+1} + C'c^{i+1} = -\sigma v^i - g^{i+1} - v_t^i, \text{ on } \gamma_{in}.$$
 (80)

Similarly, we solve for the unknown spectral coefficients a^{i+1} , b^{i+1} and c^{i+1} , using the normal equation of the LS system (79)–(80).

Remark 7 For the LS system in Case 1, Case 2: a) and Case 2: b) described above, the normal equation approach reduces the computational cost of the algorithms significantly, since the size of the normal matrices will be $L \times L$, $2L \times (2L)$ or $3L \times (3L)$, and $|\gamma_{in}| \gg L$. As for the condition numbers of the normal matrices, they can be reduced to the magnitude of approximately 10^3 on all meshes when one, for example, uses a simple preconditioner based on the maximum value in the column scaling in the LS system, i.e. for LS system Ax = b, the normal matrix is $P^T A^T A P$ where P is a diagonal matrix with $P_{ii} = 1/max(A_i)$, where A_i is the i-th column of the matrix A. See Tables 12 for examples of the condition numbers.

Once we get the spectral coefficients (see *Case 1*, *Case 2: a*) and *Case 2: b*)), we will be able to reconstruct (i) the solutions $u^{i+1}(x,y,z)$ or $v^{i+1}(x,y,z)$ for (x,y,z) on the surface at the time level t^{i+1} using the spectral approximations; and (ii) the density u_{γ}^{i+1} at time level t^{i+1} using (40) (dynamic boundary conditions), (53) (bulk-surface model with linear coupling), or (64) (bulk-surface model with nonlinear coupling). Finally, the approximated solution $u_{j,k,l}^{i+1}$, $(x_j,y_k,z_l) \in N^+$ to the model (1)-(3) or (4)-(8) at the time level t^{i+1} is obtained using the discrete generalized Green's formula (81) below.

Discrete Generalized Green's Formula. The final step of DPM is to use the computed density u_{γ}^{i+1} to construct the approximation to the continuous solution in the bulk of the model (1)-(3), or of (4)-(8).

Proposition 2 (Discrete Generalized Green's formula.) The discrete solution $u_{j,k,l}^{i+1}$ on N^+ constructed using Discrete Generalized Green's formula,

$$u_{i,k,l}^{i+1} = P_{N^+ \gamma} u_{\gamma}^{i+1} + G_{h,\Delta t} F_{i,k,l}^{i+1}, \quad (x_j, y_k, z_l) \in N^+,$$
 (81)

is the approximation to the exact solution u at $(x_j, y_k, z_l) \in \Omega$ at time t^{i+1} of the continuous model (1)-(3), or of (4)-(8). We also conjecture that we have the following accuracy of the proposed numerical scheme,

$$\left\| u_{j,k,l}^{i+1} - u(x_j, y_k, z_l, t^{i+1}) \right\|_{\infty} = O(h^2 + \Delta t^2).$$
 (82)

Remark 8 The accuracy (82) is observed in all numerical experiments presented in Section 4. The reader can consult [32] for the detailed theoretical foundation of DPM.

Algorithm 1 An Outline of Main Steps of the DPM-based Algorithm

```
1: Construct point sets M^{\pm}, M^0, N^{\pm}, N^0, \gamma_{ex} and \gamma_{in} from uniform meshes on the auxiliary domain \Omega^0, which embeds \Omega
```

- 2: Assemble matrices for the reduced BEP:
- 3: if Case 1 then
- 4: Assemble A, then compute $A P_{\gamma}A$ with restriction to the point set γ_{in} in (77)
- 5: **else if** Case 2: a) then
- 6: Assemble A and B, then compute $A P_{\gamma}A$, $B P_{\gamma}B$ with restriction to the point set γ_{in} in (78)
- 7: **else if** *Case* 2: *b*) **then**
- 8: Assemble A, B and C, then compute $A P_{\gamma}A$, $B P_{\gamma}B$, $C P_{\gamma}C$ with restriction to the point set γ_{in} in (79), and assemble A' in γ_{in}
- 9: end if
- 10: if Case 1 or Case 2: a) then
- 11: Precompute the inverse of the coefficient matrix in the normal equation of the LS system (77) or (78), using Cholesky decomposition
- 12: **end if**
- 13: Initialize the bulk/surface solutions using the initial conditions
- 14: while $t^{i+1} \leq T_{final}$ do
- 15: **if** *Case 2: b)* **then**
- 16: Assemble matrix C' in γ_{in} and compute the Cholesky decomposition of the coefficient matrix of the normal equation corresponding to the LS system (79)–(80)
- 17: end if
- 18: Construct the Particular Solution $G_{h,\Delta t}F_{j,k,l}^{i+1}$ on N^+ using the discrete AP
- 19: Solve the BEP for the unknown spectral coefficients using the normal equations
- 20: Reconstruct the density u_y^{i+1} using extension operator (40) for Case 1, (53) for Case 2: a), or (64) for Case 2: b)
- 21: Obtain bulk solution u^{i+1} using the discrete generalized Green's formula (81), and surface solution u^{i+1} or v^{i+1} using the spectral approximation
- 22: Update and march in time
- 23: end while

Remark 9 We solve the LS systems (77) in Case 1, (78) in Case 2: a), and (79)–(80) in Case 2: b) using the normal equation approach. For the normal equations of the resulting algebraic

systems, the inverse matrices of the normal matrices are pre-computed outside of the time loop for Case 1 and Case 2: a) using Cholesky decomposition.

For $Case\ 2:b$), the normal matrix needs to be assembled and the Cholesky decomposition is performed at each time step since the matrix C' is updated at each time level inside the time loop. However, if the size of the normal matrix is large, for efficiency, one can exploit the block structures of the normal matrix and update only the blocks associated with C' at each time step.

4 Numerical Results

In this section, we illustrate setup of the numerical tests and present the numerical results (errors and convergence rates, 3D views of the bulk/surface solutions, etc.) for the models with dynamic boundary condition (BC) (1)–(3), and for the bulk-surface problems (4)–(8). In this work, we restrict our discussion to a spherical domain with radius R centered at the origin. For a general domain in 3D, the proposed algorithms can be extended in a straightforward way, for example, by selecting a different set of basis functions or replacing the spectral approach on the surface with the trace-FEM [8,9] (see Remark 5 in Section 3.1), which will be reported in future work.

4.1 Setup of Numerical Tests

The auxiliary domain is chosen to be a cube, i.e., $[-R-R/5, R+R/5] \times [-R-R/5, R+R/5] \times [-R-R/5, R+R/5]$. Then, the auxiliary domain is discretized using meshes of dimension $N \times N \times N$ and the grid spacing of the mesh is h = 2(R+R/5)/N. We adopt the notation $N \times N \times N$ for meshes throughout this numerical section. Note that, other choices of the auxiliary domains will also work.

For the basis functions $\phi_{\kappa}(\theta, \varphi)$, we use the following spherical harmonics:

$$Y_{\ell}^{\mathfrak{m}}(\theta,\varphi) = \begin{cases} P_{\ell}^{\mathfrak{m}}(\cos\theta), & \mathfrak{m} = 0, \\ P_{\ell}^{\mathfrak{m}}(\cos\theta)\cos(m\varphi), & \mathfrak{m} > 0, & \text{for } -\ell \leq \mathfrak{m} \leq \ell. \\ P_{\ell}^{\mathfrak{m}}(\cos\theta)\sin(|m|\varphi), & \mathfrak{m} < 0, \end{cases}$$
(83)

where $Y_{\ell}^{\mathfrak{m}}(\theta,\varphi)$ is the spherical harmonic function of degree ℓ and order \mathfrak{m} . For the index κ in $\phi_{\kappa}(\theta,\varphi)$, it is related to (ℓ,\mathfrak{m}) , i.e.,

$$\kappa = \begin{cases} \ell^2 + 2m + 1, & m \ge 0, \\ \ell^2 + 2|m|, & m < 0, \end{cases}$$
 (84)

The total number of spherical harmonics used in the tests is determined by the exact solutions u(x, y, z, t) and v(x, y, z, t) on the boundary Γ . Generally, the spectral coefficients of the spherical harmonic basis functions for the initial data of u and v can be computed. This helps to determine the degree and the order of the spherical harmonics to be included in the spectral approximations. Thus, the total number of harmonics used in the numerical tests is independent of the grid spacing h. The only constraint on the number of the harmonics is that, the total number of unknown spectral coefficients in the BEPs ((77) for $Case\ 1$, (78) for $Case\ 2$: a), and (79) for $Case\ 2$: b)) is much less than $|\gamma_{in}|$. Generally, this condition is easily satisfied due to the abundance of mesh nodes in γ_{in} in 3D, and the relative small number of basis functions required to resolve u and v on the boundary.

In all the numerical tests in this section, we set the final time to be T=0.1. For the time approximation of the models, we adopt the second-order trapezoidal scheme, and we use the time step $\Delta t=h$, since we consider the second-order approximation in space. There is no particular reason of the choice of the trapezoidal rule, and other second-order implicit time stepping techniques can also be employed. For example, one can use the second-order implicit Runge-Kutta scheme, and the numerical results will not be significantly different from the ones obtained with the trapezoidal rule.

4.2 The Bulk/Surface Errors

The approximation to the ∞ -, L^2 - and H^1 -norm errors in the bulk are computed using the following formulas respectively:

$$||u - u_h^i||_{\infty(\Omega)} \approx E_{\infty(\Omega)} = \max_{i,i,k,l} \mathbb{1}_{M^+} \left| u^e(x_j, y_k, z_l, t^i) - u_{j,k,l}^i \right|$$
(85)

$$||u - u_h^i||_{L^2(\Omega)} \approx E_{L^2(\Omega)} = \max_i \left[\sum_{j,k,l} \mathbb{1}_{M^+} \left(u(x_j, y_k, z_l, t^i) - u_{j,k,l}^i \right)^2 h^3 \right]^{\frac{1}{2}}$$
 (86)

$$\begin{split} &||u-u_{h}^{i}||_{H^{1}(\Omega)}\approx E_{H^{1}(\Omega)}=\max_{i}\left[\sum_{j,k,l}\mathbb{1}_{M^{+}}\left(u(x_{j},y_{k},z_{l},t^{i})-u_{j,k,l}^{i}\right)^{2}h^{3}\right.\\ &+\mathbb{1}_{M^{+}}\left(\frac{u(x_{j}+h,y_{k},z_{l},t^{i})-u(x_{j}-h,y_{k},z_{l},t^{i})}{2h}-\frac{u_{j+1,k,l}^{i}-u_{j-1,k,l}^{i}}{2h}\right)^{2}h^{3}\\ &+\mathbb{1}_{M^{+}}\left(\frac{u(x_{j},y_{k}+h,z_{l},t^{i})-u(x_{j},y_{k}+h,z_{l},t^{i})}{2h}-\frac{u_{j,k+1,l}^{i}-u_{j,k-1,l}^{i}}{2h}\right)^{2}h^{3}\\ &+\mathbb{1}_{M^{+}}\left(\frac{u(x_{j},y_{k},z_{l}+h,t^{i})-u(x_{j},y_{k},z_{l}-h,t^{i})}{2h}-\frac{u_{j,k,l+1}^{i}-u_{j,k,l-1}^{i}}{2h}\right)^{2}h^{3}\right]^{\frac{1}{2}} \end{split}$$

where $u^i_{j,k,l} \approx u(x_j, y_k, z_l, t^i)$ and u^i_h denotes also the numerical approximation to the exact solution at time t^i using grid spacing h. Also, $\mathbb{1}_{M^+}$ is the characteristic function for the point set M^+ .

Additionally, we consider the ∞ -norm error for the components in the gradient of the bulk solution $u^i_{j,k,l}$ at time level t^i . For example, the ∞ -norm error of the x-component can be computed using the following formula:

$$E_{\infty(\Omega)} = \max_{i,j,k,l} \mathbb{1}_{M^+} \left| \frac{u(x_j + h, y_k, z_l, t^i) - u(x_j - h, y_k, z_l, t^i)}{2h} - \frac{u^i_{j+1,k,l} - u^i_{j-1,k,l}}{2h} \right|, \quad (88)$$

and the errors in y, z-components are computed similarly.

The approximations to the ∞ -, L^2 -norm and H^1 -norm errors on the surface are computed using the following formulas respectively:

$$||v - v_h^i||_{\infty(\Gamma)} \approx E_{\infty(\Gamma)} = \max_{i,j,k} \left| v(R, \theta_j, \varphi_k, t^i) - v_{j,k}^i \right|$$
(89)

$$||v - v_h^i||_{L^2(\Gamma)} \approx E_{L^2(\Gamma)} = \max_i \left[\sum_{j,k} \left(v(R, \theta_j, \varphi_k, t^i) - v_{j,k}^i \right)^2 \sin \theta_j \Delta \theta \Delta \varphi \right]^{\frac{1}{2}}$$
(90)

$$\begin{split} ||v-v_{h}^{i}||_{H^{1}(\Gamma)} &\approx E_{H^{1}(\Gamma)} = \max_{i} \left[\sum_{j,k} \left(v(R,\theta_{j},\varphi_{k},t^{i}) - v_{j,k}^{i} \right)^{2} \sin\theta_{j} \Delta\theta \Delta\varphi \right. \\ &+ \left(\frac{v(R,\theta_{j} + \Delta\theta,\varphi_{k},t^{i}) - v(R,\theta_{j},\varphi_{k},t^{i})}{R\Delta\theta} - \frac{v_{j+1,k}^{i} - v_{j,k}^{i}}{R\Delta\theta} \right)^{2} \sin\theta_{j} \Delta\theta \Delta\varphi \\ &+ \left(\frac{v(R,\theta_{j},\varphi_{k} + \Delta\varphi,t^{i}) - v(R,\theta_{j},\varphi_{k},t^{i})}{R\sin\theta_{j} \Delta\varphi} - \frac{v_{j,k+1}^{i} - v_{j,k}^{i}}{R\sin\theta_{j} \Delta\varphi} \right)^{2} \sin\theta_{j} \Delta\theta \Delta\varphi \right]^{\frac{1}{2}} \end{split} \tag{91}$$

where $v_{j,k}^i \approx v(R, \theta_j, \varphi_k, t^i)$ and v_h^i denotes also the numerical approximation of the exact solution at time t^i . The increments in the discretization of θ and φ are $\Delta\theta$ and $\Delta\varphi$ respectively. Moreover, in (91), we require $\sin \theta_j \neq 0$. For the surface errors of the model (1)–(3) with dynamic boundary condition, one simply replaces v with u in the formulas (89)–(91).

Note that, for all the ∞ -, L^2 - and H^1 -norm errors in space, the ∞ -norm is taken in time.

4.3 Dynamic Boundary Conditions

In this subsection, we present the numerical results for models (1)–(3) with dynamic boundary conditions in a spherical domain with radius R = 0.5.

4.3.1 Test 1

For the first test, we employ the exact solution $u(x, y, z, t) = e^t(x^2 + 2y^2 + 3z^2)$. The consideration of such a test problem is that it offers both simplicity and asymmetry in space.

In Table 1, we observe that in the bulk, the L^2 -norm errors are smaller than the ∞ errors, which is as expected. However, on the surface, the L^2 -norm errors are larger than the ∞ -norm errors. This can be explained by the following estimate of the L^2 -norm errors:

$$E_{L^{2}(\Gamma)} = \max_{i} \left[\sum_{j,k} \left(u(R, \theta_{j}, \varphi_{k}, t^{i}) - u_{j,k}^{i} \right)^{2} \sin \theta_{j} \Delta \theta \Delta \varphi \right]^{\frac{1}{2}}$$
(92)

$$\leq \max_{i,j,k} \left| u(R,\theta_j,\varphi_k,t^i) - u^i_{j,k} \right| \left[\sum_{j,k} \sin \theta_j \Delta \theta \Delta \varphi \right]^{\frac{1}{2}}$$
(93)

$$\approx \sqrt{4\pi R^2} \max_{i,i,k} \left| u(R,\theta_j,\varphi_k,t^i) - u^i_{j,k} \right| \tag{94}$$

$$=2R\sqrt{\pi}E_{\infty(\Gamma)}\tag{95}$$

We observe the overall second-order convergence in all norms of the errors for solutions, both on the surface and in the bulk. Note that, the ∞ -norm errors of the gradients in the bulk

$N \times N \times N$	$E_{\infty(\Omega)}:u$	Rate	$E_{L^2(\Omega)}:u$	Rate	$E_{H^1(\Omega)}:u$	Rate
31 × 31 × 31	5.7519 E-6		3.4724 E-6		4.7239 E-6	
$63 \times 63 \times 63$	1.6449 E-6	1.81	9.3307 E-7	1.90	1.2730 E-6	1.89
$127 \times 127 \times 127$	4.0469 E-7	2.02	2.3127 E-7	2.01	3.1149 E-7	2.03
$255 \times 255 \times 255$	1.0445 E-7	1.95	5.8647 E-8	1.98	7.9459 E-8	1.97
$N \times N \times N$	$E_{\infty(\Gamma)}:u$	Rate	$E_{L^2(\Gamma)}: u$	Rate	$E_{H^1(\Gamma)}: u$	Rate
$31 \times 31 \times 31$	5.8021 E-6	_	8.9307 E-6	_	9.6440 E-6	_
$63 \times 63 \times 63$	1.6613 E-6	1.80	2.4687 E-6	1.86	2.7621 E-6	1.80
$127 \times 127 \times 127$	4.0576 E-7	2.03	6.1087 E-7	2.01	6.7467 E-7	2.03
$255 \times 255 \times 255$	1.0469 E-7	1.95	1.5629 E-7	1.97	1.7384 E-7	1.96
$N \times N \times N$	$E_{\infty(\Omega)}: \nabla_x u$	Rate	$E_{\infty(\Omega)}: \nabla_{\mathcal{Y}} u$	Rate	$E_{\infty(\Omega)}: \nabla_z u$	Rate
$31 \times 31 \times 31$	1.8856 E-6	_	4.6662 E-6	_	7.7164 E-6	_
$63 \times 63 \times 63$	4.1092 E-7	2.20	1.1122 E-6	2.07	1.8944 E-6	2.03
$127 \times 127 \times 127$	9.8629 E-8	2.06	2.7337 E-7	2.02	4.6526 E-7	2.03
$255 \times 255 \times 255$	2.4337 E-8	2.02	6.7944 E-8	2.01	1.1611 E-7	2.00

Table 1: Convergence of the ∞ -, L^2 - and H^1 -norm errors of the solutions in the bulk/surface, and the ∞ -norm errors of the gradients in the bulk for the dynamic BC model (1)–(3) with exact solution $u = e^t(x^2 + 2y^2 + 3z^2)$ until final time T = 0.1 in the sphere of R = 0.5. The number of spherical harmonics for term u is 9.

$N \times N \times N$	$E_{\infty(\Omega)}:u$	Rate	$E_{L^2(\Omega)}:u$	Rate	$E_{H^1(\Omega)}:u$	Rate
$31 \times 31 \times 31$	1.6347 E-4	_	4.8011 E-5	_	2.9914 E-4	_
$63 \times 63 \times 63$	2.4156 E-5	2.76	6.4637 E-6	2.89	4.9519 E-5	2.59
$127 \times 127 \times 127$	3.4620 E-6	2.80	9.1209 E-7	2.83	8.3727 E-6	2.56
$255 \times 255 \times 255$	5.5230 E-7	2.65	1.4151 E-7	2.69	1.4736 E-6	2.51
$N \times N \times N$	$E_{\infty(\Gamma)}:u$	Rate	$E_{L^2(\Gamma)}:u$	Rate	$E_{H^1(\Gamma)}:u$	Rate
$31 \times 31 \times 31$	1.6052 E-5	_	1.1379 E-5	_	3.3818 E-5	_
$63 \times 63 \times 63$	3.0297 E-6	2.41	3.0092 E-6	1.92	5.5188 E-6	2.62
$127 \times 127 \times 127$	4.7815 E-7	2.66	6.9355 E-7	2.12	8.9181 E-7	2.63
$255 \times 255 \times 255$	1.1105 E-7	2.11	1.6069 E-7	2.11	1.7645 E-7	1.96
$N \times N \times N$	$E_{\infty(\Omega)}: \nabla_x u$	Rate	$E_{\infty(\Omega)}: \nabla_{\mathcal{Y}} u$	Rate	$E_{\infty(\Omega)}: \nabla_z u$	Rate
$31 \times 31 \times 31$	1.8435 E-3	_	1.8622 E-3	_	1.8753 E-3	_
$63 \times 63 \times 63$	4.8836 E-4	1.92	4.5222 E-4	2.04	4.6395 E-4	2.02
$127 \times 127 \times 127$	1.2831 E-4	1.93	1.1405 E-4	1.99	1.0923 E-4	2.09
$255 \times 255 \times 255$	3.4607 E-5	1.89	3.2892 E-5	1.79	3.1182 E-5	1.81

Table 2: Convergence: d perturbed by ϵh^3 for for the dynamic BC model (1)–(3) with exact solution $u = e^t(x^2 + 2y^2 + 3z^2)$ until final time T = 0.1 in the sphere of R = 0.5. The number of spherical harmonics for term u is 9.

also obey the second-order convergence, as well as the H^1 -norm errors in the bulk and on the surface.

In Tables 2–5, we present the convergence results for the dynamic BC model (1)–(3) with perturbed d, θ , and φ in the extension operator (28). (The perturbations in θ and φ mimic the "errors" in the normal vector n.) We investigated numerically with different choices of perturbations and present the results with ϵh^3 (ϵ is a pseudo-random number sampled uniformly from [0, 1]), which preserves the second-order accuracy of the solution in ∞ -, L^2 - and H^1 -norm, and the gradient components in ∞ -norm. Since the random perturbation is

$N \times N \times N$	$E_{\infty(\Omega)}:u$	Rate	$E_{L^2(\Omega)}:u$	Rate	$E_{H^1(\Omega)}:u$	Rate
$31 \times 31 \times 31$	3.1314 E-5	_	5.5099 E-6	_	5.8781 E-5	
$63 \times 63 \times 63$	4.9768 E-6	2.65	1.0797 E-6	2.35	1.1369 E-5	2.37
$127 \times 127 \times 127$	9.7584 E-7	2.35	2.3402 E-7	2.21	2.2574 E-6	2.33
$255 \times 255 \times 255$	1.8121 E-7	2.43	5.9103 E-8	1.99	4.7119 E-7	2.26
$N \times N \times N$	$E_{\infty(\Gamma)}:u$	Rate	$E_{L^2(\Gamma)}:u$	Rate	$E_{\boldsymbol{H}^1(\Gamma)}:u$	Rate
$31 \times 31 \times 31$	3.0261 E-5	_	2.6860 E-5	_	7.6184 E-5	_
$63 \times 63 \times 63$	4.7251 E-6	2.68	4.0207 E-6	2.74	9.6476 E-6	2.98
$127 \times 127 \times 127$	7.7908 E-7	2.61	7.1346 E-7	2.49	1.3434 E-6	2.84
$255 \times 255 \times 255$	1.5157 E-7	2.36	1.6333 E-7	2.13	2.2525 E-7	2.58
$N \times N \times N$	$E_{\infty(\Omega)}: \nabla_x u$	Rate	$E_{\infty(\Omega)}: \nabla_{\mathcal{Y}} u$	Rate	$E_{\infty(\Omega)}: \nabla_z u$	Rate
$31 \times 31 \times 31$	4.7534 E-4	_	3.6962 E-4	_	4.0036 E-4	
$63 \times 63 \times 63$	1.3972 E-4	1.77	1.0855 E-4	1.77	1.2844 E-4	1.64
$127 \times 127 \times 127$	3.7348 E-5	1.90	2.8852 E-5	1.91	3.4981 E-5	1.88
$255 \times 255 \times 255$	1.0169 E-5	1.88	7.8385 E-6	1.88	9.6735 E-6	1.85

Table 3: Convergence: θ perturbed by ϵh^3 for for the dynamic BC model (1)–(3) with exact solution $u = e^t(x^2 + 2y^2 + 3z^2)$ until final time T = 0.1 in the sphere of R = 0.5. The number of spherical harmonics for term u is 9.

$N \times N \times N$	$E_{\infty(\Omega)}:u$	Rate	$E_{L^2(\Omega)}: u$	Rate	$E_{H^1(\Omega)}: u$	Rate
$31 \times 31 \times 31$	1.2008 E-5	_	3.5593 E-6	_	2.1347 E-5	
$63 \times 63 \times 63$	2.2351 E-6	2.43	9.5723 E-7	2.89	4.1701 E-6	2.59
$127 \times 127 \times 127$	4.8683 E-7	2.20	2.3412 E-7	2.83	7.9991 E-7	2.56
$255 \times 255 \times 255$	1.0523 E-7	2.21	5.8696 E-8	2.69	1.5425 E-7	2.51
$N \times N \times N$	$E_{\infty(\Gamma)}:u$	Rate	$E_{L^2(\Gamma)}:u$	Rate	$E_{H^1(\Gamma)}: u$	Rate
$31 \times 31 \times 31$	1.3088 E-5	_	1.1687 E-5	_	3.8782 E-5	
$63 \times 63 \times 63$	2.2948 E-6	2.51	2.6848 E-6	1.92	5.2359 E-6	2.62
$127 \times 127 \times 127$	4.4200 E-7	2.38	6.2695 E-7	2.12	8.5292 E-7	2.63
$255 \times 255 \times 255$	1.0517 E-7	2.07	1.5687 E-7	2.11	1.8487 E-7	1.96
$N \times N \times N$	$E_{\infty(\Omega)}: \nabla_x u$	Rate	$E_{\infty(\Omega)}: \nabla_{\mathcal{Y}} u$	Rate	$E_{\infty(\Omega)}: \nabla_z u$	Rate
$31 \times 31 \times 31$	1.6985 E-4	_	1.6487 E-4	_	1.4704 E-4	_
$63 \times 63 \times 63$	4.8808 E-5	1.92	5.2182 E-5	2.04	4.5240 E-5	2.02
$127 \times 127 \times 127$	1.4275 E-5	1.93	1.4329 E-5	1.99	1.2582 E-5	2.09
$255 \times 255 \times 255$	3.9625 E-6	1.89	3.9751 E-6	1.79	3.6156 E-6	1.81

Table 4: Convergence: φ perturbed by ϵh^3 for for the dynamic BC model (1)–(3) with exact solution $u = e^t(x^2 + 2y^2 + 3z^2)$ until final time T = 0.1 in the sphere of R = 0.5. The number of spherical harmonics for term u is 9.

added at every point in γ set, the total perturbation is in the order of O(h). Note that tests with perturbations in Tables 2–5 illustrate that the proposed DPM-based algorithm preserves the second-order accuracy even in situations where the signed distances and the normal vectors to the surface boundary are not known exactly.

In Fig. 2, we observe that the behavior of the L^2 - and H^1 -norm errors are very similar in the bulk and on the surface. Besides, the errors in the bulk are smaller than the errors on the surface in both norms. Also, as already mentioned, the H^1 -norm errors give the second-order convergence, as opposed to the results obtained, for example, from the finite element method, e.g., [20]. Moreover, the errors are far below the reference dashed lines, which implies a

$N \times N \times N$	$E_{\infty(\Omega)}:u$	Rate	$E_{L^2(\Omega)}:u$	Rate	$E_{H^1(\Omega)}:u$	Rate
$31 \times 31 \times 31$	1.6943 E-4	_	4.8339 E-5	_	3.0187 E-4	_
$63 \times 63 \times 63$	2.4949 E-5	2.76	6.5310 E-6	2.89	5.0688 E-5	2.59
$127 \times 127 \times 127$	3.4388 E-6	2.80	9.1301 E-7	2.83	8.6516 E-6	2.56
$255 \times 255 \times 255$	5.5585 E-7	2.65	1.4177 E-7	2.69	1.5262 E-6	2.51
$N \times N \times N$	$E_{\infty(\Gamma)}:u$	Rate	$E_{L^2(\Gamma)}: u$	Rate	$E_{H^1(\Gamma)}: u$	Rate
$31 \times 31 \times 31$	3.0730 E-5	_	2.6648 E-5	_	8.3318 E-5	_
$63 \times 63 \times 63$	4.4242 E-6	2.41	3.8308 E-6	1.92	8.5970 E-6	2.62
$127 \times 127 \times 127$	8.4725 E-7	2.66	8.1565 E-7	2.12	1.5920 E-6	2.63
$255 \times 255 \times 255$	1.4816 E-7	2.11	1.6760 E-7	2.11	2.3146 E-7	1.96
$N \times N \times N$	$E_{\infty(\Omega)}: \nabla_x u$	Rate	$E_{\infty(\Omega)}: \nabla_{\mathcal{Y}} u$	Rate	$E_{\infty(\Omega)}: \nabla_z u$	Rate
$31 \times 31 \times 31$	2.0305 E-3	_	1.7989 E-3	_	1.7563 E-3	_
$63 \times 63 \times 63$	5.5069 E-4	1.92	5.0127 E-4	2.04	5.0564 E-4	2.02
$127 \times 127 \times 127$	1.3554 E-4	1.93	1.2851 E-4	1.99	1.2397 E-4	2.09
$255 \times 255 \times 255$	3.9576 E-5	1.89	3.5780 E-5	1.79	3.2330 E-5	1.81

Table 5: Convergence: d, θ , φ perturbed by ϵh^3 for for the dynamic BC model (1)–(3) with exact solution $u = e^t(x^2 + 2y^2 + 3z^2)$ until final time T = 0.1 in the sphere of R = 0.5. The number of spherical harmonics for term u is 9.

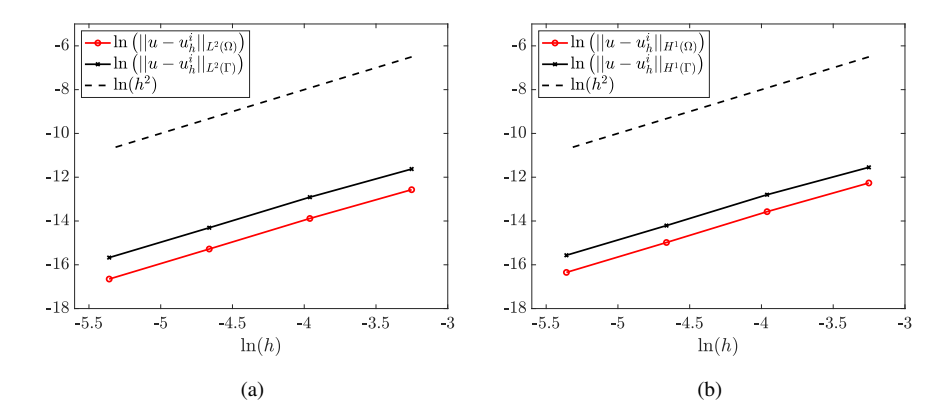
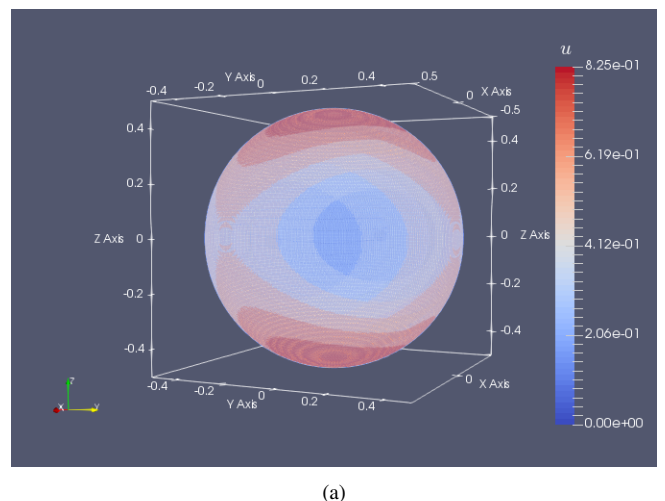


Fig. 2: Log-log plots of bulk/surface L^2 -norm errors (left figure) and bulk/surface H^1 -norm errors (right figure) for the dynamic BC model (1)–(3) with the exact solution $u = e^t(x^2 + 2y^2 + 3z^2)$ in the sphere of R = 0.5.

small error constant in (82). In Fig. 3, we show the 3D isosurface plots (analogous to the contour plots in 2D) in the top figure and the plot of surface solution in the bottom figure, obtained using mesh $255 \times 255 \times 255$ at the final time T = 0.1.

4.3.2 Test 2

In this subsection, we use the exact solution $u(x, y, z, t) = e^t \sin(x) \sin(2y) \sin(3z)$. Compared to the first test, this choice of test is more oscillatory and requires a larger number of spherical harmonics to resolve u and u_{rr} accurately on the boundary Γ . Nevertheless, the total number of harmonics is still much less than $|\gamma_{in}|$, see Table 6, for example.



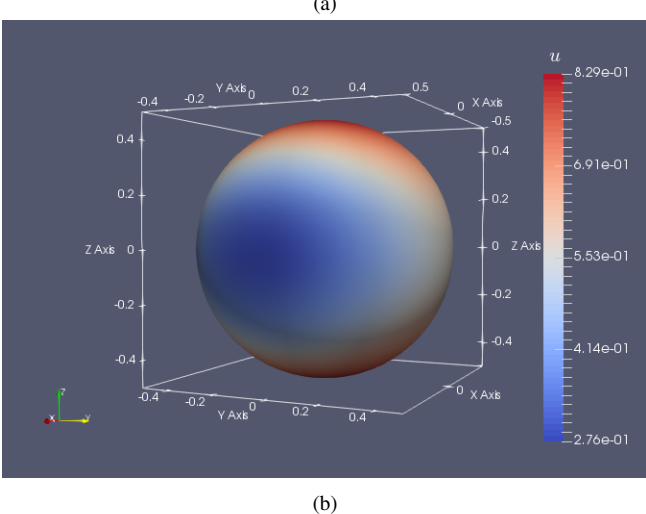


Fig. 3: 3D views of the bulk (top figure) and the surface (bottom figure) approximations from mesh $255 \times 255 \times 255$ at T = 0.1 to the dynamic BC model (1)–(3) with the exact solution $u = e^t(x^2 + 2y^2 + 3z^2)$ in the sphere of R = 0.5.

In Table 6, again we observe second-order accuracy in all norms of the solutions in the bulk and on the surface.

Similarly, in Fig. 4, the errors in the bulk are smaller than the errors on the surface. In Fig. 5, we give the 3D isosurface plots in the top figure and the plot of surface solution in the bottom figure, obtained using mesh $255 \times 255 \times 255$ at final time T = 0.1.

4.4 Linear Bulk-Surface Coupling

In this subsection, we present the numerical results for the model (4)–(8), with linear bulksurface coupling, i.e., h(u, v) = u - v in a spherical domain of radius R = 1. In particular, the

$N \times N \times N$	$E_{\infty(\Omega)}:u$	Rate	$E_{L^2(\Omega)}:u$	Rate	$E_{H^1(\Omega)}:u$	Rate
$31 \times 31 \times 31$	8.7147 E-6	_	2.4039 E-6	_	2.8357 E-5	_
$63 \times 63 \times 63$	1.7811 E-6	2.29	5.3478 E-7	2.17	5.6563 E-6	2.33
$127 \times 127 \times 127$	4.3585 E-7	2.03	1.3077 E-7	2.03	1.3353 E-6	2.08
$255 \times 255 \times 255$	1.0849 E-7	2.01	3.2659 E-8	2.00	3.3032 E-7	2.02
$N \times N \times N$	$E_{\infty(\Gamma)}:u$	Rate	$E_{L^2(\Gamma)}:u$	Rate	$E_{H^1(\Gamma)}: u$	Rate
$31 \times 31 \times 31$	5.8527 E-6	_	5.1084 E-6	_	3.7771 E-5	_
$63 \times 63 \times 63$	1.4134 E-6	2.05	1.2405 E-6	2.04	9.0795 E-6	2.06
$127 \times 127 \times 127$	3.4714 E-7	2.03	3.0530 E-7	2.02	2.2280 E-6	2.03
$255 \times 255 \times 255$	8.5729 E-8	2.02	7.5389 E-8	2.02	5.5028 E-7	2.02
$N \times N \times N$	$E_{\infty(\Omega)}: \nabla_x u$	Rate	$E_{\infty(\Omega)}: \nabla_{\mathcal{Y}} u$	Rate	$E_{\infty(\Omega)}: \nabla_z u$	Rate
$31 \times 31 \times 31$	8.5641 E-5	_	9.0012 E-5	_	1.6055 E-4	_
$63 \times 63 \times 63$	2.3716 E-5	1.85	2.0313 E-5	2.15	5.1744 E-5	1.63
$127 \times 127 \times 127$	5.0683 E-6	2.27	5.2314 E-6	1.96	1.1111 E-5	2.22
$255 \times 255 \times 255$	1.3229 E-6	1.94	1.1629 E-6	2.17	2.8860 E-6	1.94

Table 6: Convergence of the ∞ -, L^2 - and H^1 -norm errors of the solutions in the bulk/surface, and the ∞ -norm errors of gradients in the bulk for the dynamic BC model (1)–(3) with the exact solution $u = e^t \sin(x) \sin(2y) \sin(3z)$ until final time T = 0.1 in the sphere of R = 0.5. The number of spherical harmonics for terms u is 400 per each term.

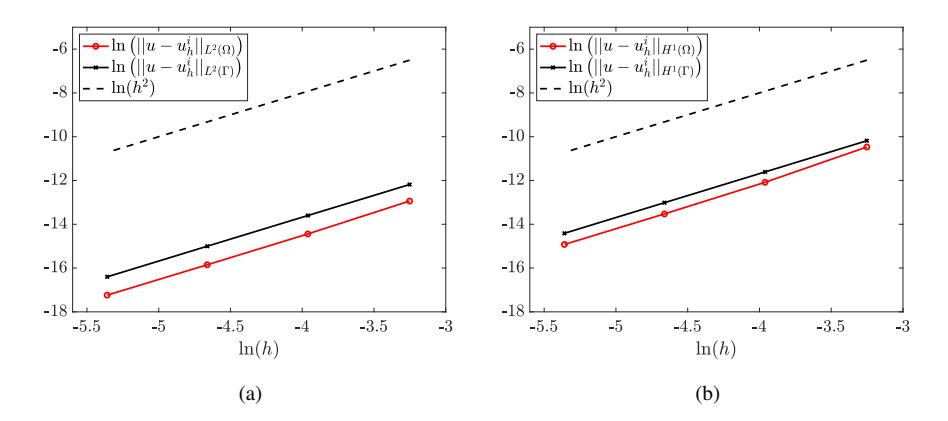


Fig. 4: Log-log plots of bulk/surface L^2 -norm errors (left figure) and bulk/surface H^1 -norm errors (right figure) for the dynamic BC model (1)–(3) with the exact solution $u = e^t \sin(x) \sin(2y) \sin(3z)$ in the sphere of R = 0.5.

exact solutions $u(x, y, z, t) = e^t e^{-x(x-1)-y(y-1)}$ and $v(x, y, z, t) = e^t e^{-x(x-1)-y(y-1)}(1 + x(1 - 2x) + y(1 - 2y))$ are such that the coupling condition (5) is satisfied exactly on the surface (the test is modification of the tests from [6, 14]). Additionally, we provide numerical results to compare with the ones obtained using the cut finite element method in [6].

Remark 10 We should note that the comparisons between the DPM-based method in this work and the cut-FEM approach in [6] are not precise, since the exact solutions $u(x, y, z) = e^{-x(x-1)-y(y-1)}$ and $v(x, y, z) = e^{-x(x-1)-y(y-1)}(1+x(1-2x)+y(1-2y))$ in [6] are considered for the elliptic type bulk-surface problems. Nevertheless, we add e^t in the exact solutions and

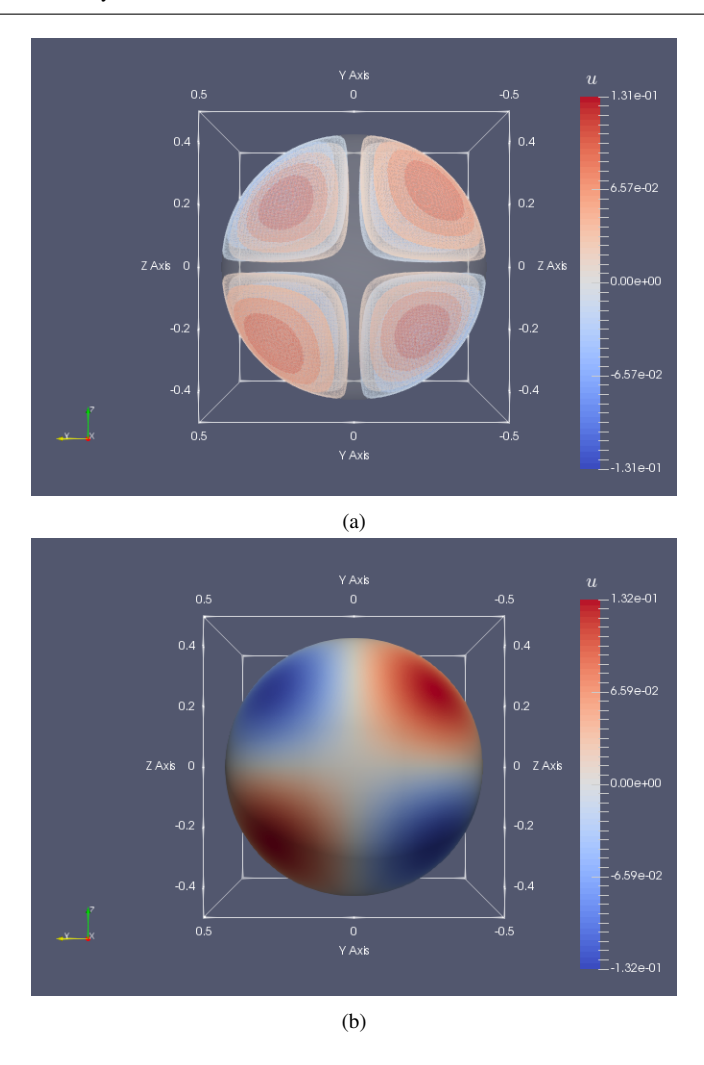


Fig. 5: 3D views of the bulk (top figure) and the surface (bottom figure) approximations from mesh $255 \times 255 \times 255$ at T = 0.1 to the dynamic BC model (1)–(3) with the exact solution $u = e^t \sin(x) \sin(2y) \sin(3z)$ in the sphere of R = 0.5.

take the ∞ -norm errors in time, in the hope to discuss the difference and similarity between the two approaches.

In Table 7, we observe second-order accuracy for all norms of the solutions in the bulk and on the surface, together with the second-order accuracy in the components of the gradients. The relative larger errors of L^2 -norm on the surface, compared to the ∞ -norm, again can be similarly explained by the inequalities (92)–(95).

In Fig. 6, we observe second-order convergence for both the L^2 - and H^1 -norm errors in the bulk and on the surface. In contrast, the bulk/surface H^1 -norm errors in the cut finite element approach [6, Fig. 4] are only first order accurate. Furthermore, compared to [6, Fig.

$N \times N \times N$	$E_{\infty(\Omega)}:u$	Rate	$E_{L^2(\Omega)}:u$	Rate	$E_{H^1(\Omega)}:u$	Rate
31 × 31 × 31	1.2537 E-3	_	9.5344 E-4	_	3.5388 E-3	_
$63 \times 63 \times 63$	2.9791 E-4	2.07	2.2803 E-4	2.06	7.0225 E-4	2.33
$127 \times 127 \times 127$	7.2333 E-5	2.04	5.5188 E-5	2.05	1.7337 E-4	2.02
$255 \times 255 \times 255$	1.7734 E-5	2.03	1.3555 E-5	2.03	4.2658 E-5	2.02
$N \times N \times N$	$E_{\infty(\Gamma)}: v$	Rate	$E_{L^2(\Gamma)}: v$	Rate	$E_{\boldsymbol{H}^1(\Gamma)}:v$	Rate
31 × 31 × 31	9.3119 E-5	_	1.2573 E-4	_	2.9557 E-4	_
$63 \times 63 \times 63$	2.3982 E-5	1.96	3.2923 E-5	1.93	7.3660 E-5	2.00
$127 \times 127 \times 127$	6.3155 E-6	1.93	8.5321 E-6	1.95	1.9781 E-5	1.90
$255 \times 255 \times 255$	1.5774 E-6	2.00	2.1147 E-6	2.01	4.9585 E-6	2.00
$N \times N \times N$	$E_{\infty(\Omega)}: \nabla_x u$	Rate	$E_{\infty(\Omega)}: \nabla_{\mathcal{Y}} u$	Rate	$E_{\infty(\Omega)}: \nabla_z u$	Rate
$31 \times 31 \times 31$	8.2067 E-3	_	8.2067 E-3	_	2.5934 E-3	_
$63 \times 63 \times 63$	1.1452 E-3	2.84	1.1452 E-3	2.84	3.6088 E-4	2.85
$127 \times 127 \times 127$	2.9309 E-4	1.97	2.9309 E-4	1.97	6.3228 E-5	2.51
$255 \times 255 \times 255$	7.6635 E-5	1.94	7.6635 E-5	1.94	1.5690 E-5	2.01

Table 7: Convergence of the ∞ -, L^2 - and H^1 -norm errors of the solutions in the bulk/surface, and the ∞ -norm errors of gradients in the bulk for the model (4)–(8) with linear bulk-surface coupling. The exact solutions are $u=e^te^{-x(x-1)-y(y-1)}$ and $v=e^te^{-x(x-1)-y(y-1)}(1+x(1-2x)+y(1-2y))$ until final time T=0.1 in the sphere of R=1. The number of spherical harmonics for terms v and u_{rr} is 529 per each term.

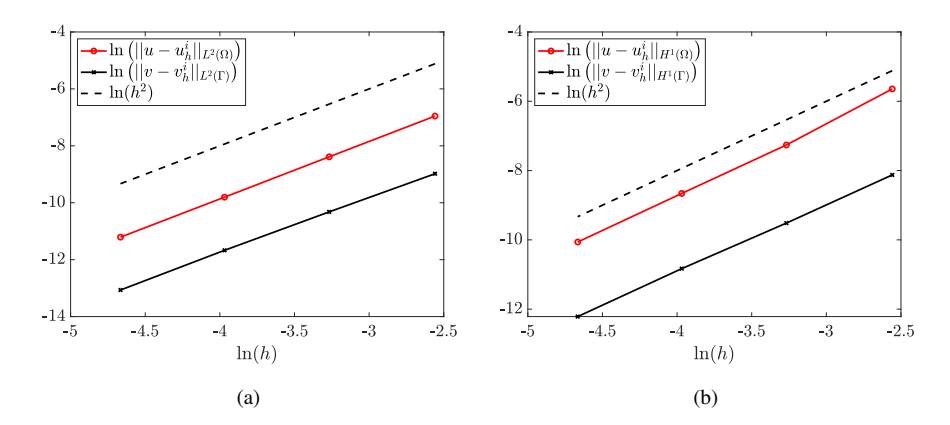


Fig. 6: Log-log plots of bulk/surface L^2 -norm errors (left figure) and bulk/surface H^1 -norm errors (right figure) for the model (4)–(8) with linear bulk-surface coupling h(u, v) = u - v. The exact solutions are $u = e^t e^{-x(x-1)-y(y-1)}$ and $v = e^t e^{-x(x-1)-y(y-1)}(1+x(1-2x)+y(1-2y))$ with final time T = 0.1 in the sphere of R = 1.

4], the approach based on DPM in this work gives much smaller L^2 -norm errors both in the bulk and on the surface.

In the meantime, we notice that in Fig. 6, the errors on the surface are smaller than the errors in the bulk, which is different from the results of the models with dynamic boundary conditions, see Figs. 2 and 4. Nevertheless, the second-order convergence rates are recovered in all cases.

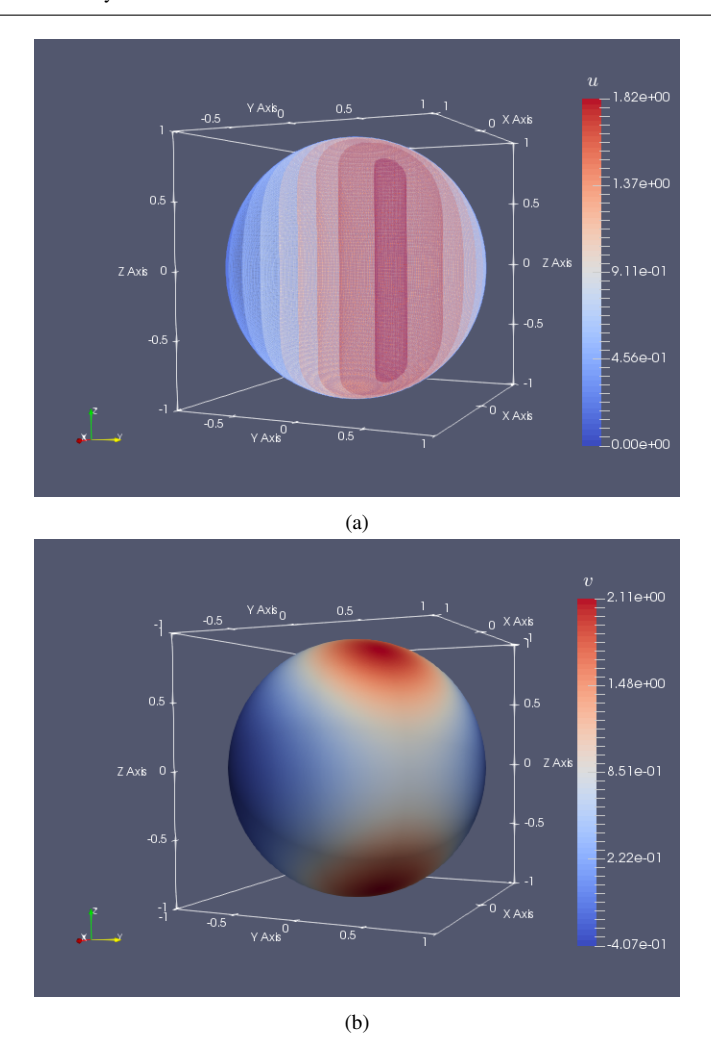


Fig. 7: 3D views of the bulk (top figure) and the surface (bottom figure) approximations from mesh $255 \times 255 \times 255$ at T=0.1 to the model (4)–(8) with linear bulk-surface coupling h(u,v)=u-v. The exact solutions are $u=e^te^{-x(x-1)-y(y-1)}$, $v=e^te^{-x(x-1)-y(y-1)}(1+x(1-2x)+y(1-2y))$ in the sphere of R=1.

In Fig. 7, we illustrate the solution via the 3D isosurface plots in the top figure and the plot of the surface solution in the bottom figure, obtained on mesh $255 \times 255 \times 255$ at final time T=0.1. The bottom figure in Fig. 7 can also be compared to [6, Fig. 3]. In this work, we are able to recover a better resolution of the solution on the surface using the DPM-based algorithms.

$N \times N \times N$	$E_{\infty(\Omega)}:u$	Rate	$E_{L^2(\Omega)}:u$	Rate	$E_{H^1(\Omega)}:u$	Rate
31 × 31 × 31	2.1745 E-3	_	1.4171 E-3	_	4.5547 E-3	_
$63 \times 63 \times 63$	6.6223 E-4	1.72	4.0246 E-4	1.82	1.1225 E-3	2.02
$127 \times 127 \times 127$	1.8343 E-4	1.85	1.0690 E-4	1.91	3.1453 E-4	1.84
$255 \times 255 \times 255$	4.6212 E-5	1.99	2.7124 E-5	1.98	7.8796 E-5	2.00
$N \times N \times N$	$E_{\infty(\Gamma)}: v$	Rate	$E_{L^2(\Gamma)}: v$	Rate	$E_{H^1(\Gamma)}: v$	Rate
31 × 31 × 31	1.2462 E-4	_	1.7529 E-4	_	3.6232 E-4	_
$63 \times 63 \times 63$	5.6149 E-5	1.15	7.6767 E-5	1.19	1.5940 E-4	1.18
$127 \times 127 \times 127$	1.7791 E-5	1.66	2.3819 E-5	1.69	4.9687 E-5	1.68
$255 \times 255 \times 255$	4.6461 E-6	1.94	6.3801 E-6	1.90	1.2982 E-5	1.94
$N \times N \times N$	$E_{\infty(\Omega)}: \nabla_x u$	Rate	$E_{\infty(\Omega)}: \nabla_{\mathcal{Y}} u$	Rate	$E_{\infty(\Omega)}: \nabla_z u$	Rate
$31 \times 31 \times 31$	8.5460 E-3	_	8.5460 E-3		4.2336 E-3	_
$63 \times 63 \times 63$	1.0922 E-3	2.97	1.0922 E-3	2.97	1.3177 E-3	1.68
$127 \times 127 \times 127$	3.1575 E-4	1.79	3.1575 E-4	1.79	3.6751 E-4	1.84
$255 \times 255 \times 255$	7.5933 E-5	2.06	7.5933 E-5	2.06	9.9683 E-5	1.88

Table 8: Convergence of the ∞ -, L^2 - and H^1 -norm errors of the solutions in the bulk/surface, and the ∞ -norm errors of gradients in the bulk for the model (4)–(8) with nonlinear bulk-surface coupling. The exact solutions are $u=e^te^{-x(x-1)-y(y-1)}$ and $v=e^te^{-x(x-1)-y(y-1)}(1+x(1-2x)+y(1-2y))$ until final time T=0.1 in the sphere of R=1. The number of spherical harmonics for terms u,v and u_{rr} is 529 per each term, and $v^{i+1}\approx v^i+\Delta t v^i_t$.

4.5 Nonlinear Bulk-Surface Coupling

In this subsection, we demonstrate the numerical results for the models (4)–(8) with nonlinear bulk-surface coupling h(u, v) = uv in the spherical domain of radius R = 1. The considered model is motivated by the examples of the nonlinear bulk-surface coupling from [15, 20].

4.5.1 Test 1 for Nonlinear Coupling

As a first test here, we consider the exact solutions $u(x, y, z, t) = e^t e^{-x(x-1)-y(y-1)}$ in the bulk and $v(x, y, z, t) = e^t e^{-x(x-1)-y(y-1)}(1 + x(1-2x) + y(1-2y))$ on the surface. The motivation to use the same exact solutions as in the linear coupling is that, we can compare the performance of the algorithm for linear/nonlinear bulk-surface coupling and test the robustness of the numerical algorithm based on DPM.

Note that, we do not have exact nonlinear coupling as in (5) if we use the above exact solutions. Instead, we need to supply a source function w in the coupling, i.e.,

$$-n \cdot \nabla u = uv + w, \quad (x, y, z, t) \in \Gamma \times \mathbb{R}^+.$$
 (96)

Here, the source function w is computed from the exact solutions u and v. The discrete version of (96) is

$$-n \cdot \nabla u^{i+1} = u^{i+1} v^{i+1} + w^{i+1}$$
 (97)

which can be linearized, if the term v^{i+1} is approximated by either the 2-term approximation (69), or the 3-term approximation (76).

The errors in Table 8 correspond to 2-term approximation (69) for v^{i+1} . With the 2-term approximation (69), the ∞ -, L^2 -, H^1 -norm errors of solutions in the bulk and ∞ -norm errors

$N \times N \times N$	$E_{\infty(\Omega)}:u$	Rate	$E_{L^2(\Omega)}:u$	Rate	$E_{H^1(\Omega)}:u$	Rate
$31 \times 31 \times 31$	1.2442 E-3	_	9.5589 E-4	_	3.6512 E-3	_
$63 \times 63 \times 63$	3.0007 E-4	2.05	2.2875 E-4	2.06	7.1388 E-4	2.35
$127 \times 127 \times 127$	7.2477 E-5	2.05	5.4911 E-5	2.06	1.7713 E-4	2.01
$255 \times 255 \times 255$	1.7687 E-5	2.03	1.3390 E-5	2.04	4.3475 E-5	2.03
$N \times N \times N$	$E_{\infty(\Gamma)}: v$	Rate	$E_{L^2(\Gamma)}: v$	Rate	$E_{\boldsymbol{H}^1(\Gamma)}:v$	Rate
$31 \times 31 \times 31$	1.1314 E-4	_	1.3360 E-4	_	2.9799 E-4	_
$63 \times 63 \times 63$	2.9023 E-5	1.96	3.4459 E-5	1.96	7.6480 E-5	1.96
$127 \times 127 \times 127$	7.7800 E-6	1.90	9.2502 E-6	1.90	2.0684 E-5	1.89
$255 \times 255 \times 255$	1.9908 E-6	1.97	2.3611 E-6	1.97	5.2992 E-6	1.96
$N \times N \times N$	$E_{\infty(\Omega)}: \nabla_x u$	Rate	$E_{\infty(\Omega)}: \nabla_{\mathcal{Y}} u$	Rate	$E_{\infty(\Omega)}: \nabla_z u$	Rate
$31 \times 31 \times 31$	8.5799 E-3	_	8.5799 E-3	_	2.4914 E-3	
$63 \times 63 \times 63$	1.1211 E-3	2.94	1.1211 E-3	2.94	4.0347 E-4	2.63
$127 \times 127 \times 127$	2.9313 E-4	1.94	2.9313 E-4	1.94	1.0618 E-4	1.93
$255 \times 255 \times 255$	7.6440 E-5	1.94	7.6440 E-5	1.94	2.6384 E-5	2.01

Table 9: Convergence of the ∞ -, L^2 - and H^1 -norm errors of the solutions in the bulk/surface, and the ∞ -norm errors of gradients in the bulk for the model (4)–(8) with nonlinear bulk-surface coupling. The exact solutions are $u=e^te^{-x(x-1)-y(y-1)}$ and $v=e^te^{-x(x-1)-y(y-1)}(1+x(1-2x)+y(1-2y))$ until final time T=0.1 in the sphere of R=1. The number of spherical harmonics for terms u, v and u_{rr} is 529 per each term, and $v^{i+1} \approx v^i + \Delta t v^i_t + \Delta t^2 v^i_{tr}/2$.

of the gradients in the bulk all obey optimal second-order convergence. Meanwhile, the ∞ -, L^2 -, H^1 -norm errors of the solution on the surface give sub-optimal second-order accuracy in the first few coarser meshes. However, the second-order accuracy is recovered on finer meshes, e.g., on mesh $255 \times 255 \times 255$.

In Table 9, we adopt the 3-term approximation (76) for the v^{i+1} term. There are slight improvements of the accuracy for the solutions and gradients in the bulk. In the meantime, the accuracy of the solution on the surface is improved and second-order accuracy is recovered even on coarser meshes. Note that, there are barely any added computational cost, when one switches from using 2-term approximation (69) to 3-term approximation (76) for the v^{i+1} term.

Moreover, the errors in the bulk and on the surface for the nonlinear bulk-surface coupling in Table 9 are very similar to the errors for linear bulk-surface coupling in Table 7. This illustrates the robustness of the designed DPM-based algorithm. Also note that, the algorithm for nonlinear coupling is very similar to the ones for linear coupling. The only difference is that the matrix C' in the least square system (80) needs to be updated and the resulting normal matrices need to be inverted at each time step, which makes it more expensive. Hence, it is advantageous to use the reduced BEPs as it is done in the current work.

Again, the plots of L^2 - and H^1 -norm errors of the nonlinear coupling in Fig. 8 are similar to the plots of errors in the linear coupling, see Fig. 6. In Fig. 9, there is no observable difference in the isosurface plots in the bulk and the surface plots from the plots for the linear-coupling case, obtained on mesh $255 \times 255 \times 255$ at final time T = 0.1, see Fig. 7.

4.5.2 Test 2 for Nonlinear Coupling

In this subsection, we employ the exact solutions $u = v = e^t \sin(x) \sin(2y) \sin(3z)$ both in the bulk and on the surface, as the ones we use in the second test of the models with

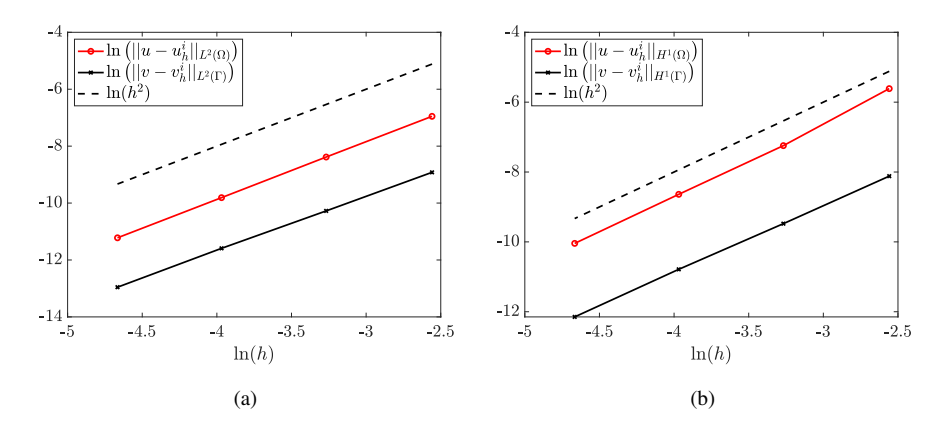


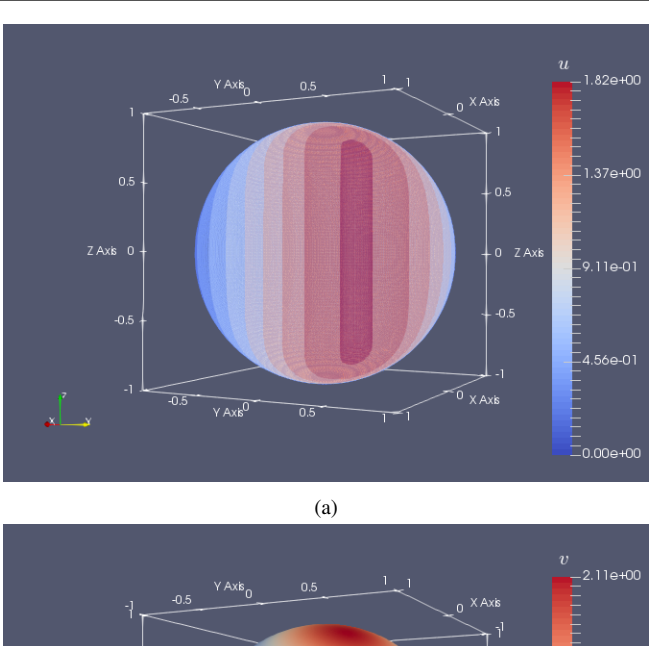
Fig. 8: Log-log plots of bulk/surface L^2 -norm errors (left figure) and bulk/surface H^1 -norm errors (right figure) for the model (4)–(8) with nonlinear bulk-surface coupling h(u,v)=uv. The exact solutions are $u=e^te^{-x(x-1)-y(y-1)}$ and $v=e^te^{-x(x-1)-y(y-1)}(1+x(1-2x)+y(1-2y))$ until final time T=0.1 in the sphere of R=1, and $v^{i+1}\approx v^i+\Delta t v^i_t+\Delta t^2 v^i_{tt}/2$.

$N \times N \times N$	$E_{\infty(\Omega)}:u$	Rate	$E_{L^2(\Omega)}:u$	Rate	$E_{H^1(\Omega)}: u$	Rate
31 × 31 × 31	1.3914 E-3		1.0543 E-3		5.0230 E-3	
$63 \times 63 \times 63$	3.6065 E-4	1.95	2.6657 E-4	1.98	1.2706 E-3	1.98
$127 \times 127 \times 127$	9.4354 E-5	1.93	6.6522 E-5	2.00	3.1710 E-4	2.00
$255 \times 255 \times 255$	2.3408 E-5	2.01	1.6608 E-5	2.00	7.9165 E-5	2.00
$N \times N \times N$	$E_{\infty(\Gamma)}: v$	Rate	$E_{L^2(\Gamma)}: v$	Rate	$E_{H^1(\Gamma)}: v$	Rate
$31 \times 31 \times 31$	2.1011 E-5	_	2.7089 E-5	_	9.9342 E-5	_
$63 \times 63 \times 63$	6.5900 E-6	1.67	7.7509 E-6	1.81	2.6332 E-5	1.92
$127 \times 127 \times 127$	1.8191 E-6	1.86	2.3303 E-6	1.73	7.1906 E-6	1.87
$255 \times 255 \times 255$	4.6581 E-7	1.97	6.0249 E-7	1.95	1.8064 E-6	1.99
$N \times N \times N$	$E_{\infty(\Omega)}: \nabla_x u$	Rate	$E_{\infty(\Omega)}: \nabla_{\mathcal{Y}} u$	Rate	$E_{\infty(\Omega)}: \nabla_z u$	Rate
$31 \times 31 \times 31$	3.3321 E-3	_	4.5730 E-3	_	4.9888 E-3	_
$63 \times 63 \times 63$	8.3625 E-4	1.99	1.0630 E-3	2.11	1.1784 E-3	2.08
$127 \times 127 \times 127$	2.0870 E-4	2.00	2.6904 E-4	1.98	2.8762 E-4	2.03
$255 \times 255 \times 255$	5.2251 E-5	2.00	6.7303 E-5	2.00	7.3246 E-5	1.97

Table 10: Convergence of the ∞ -, L^2 - and H^1 -norm errors of the solutions in the bulk/surface, and the ∞ -norm errors of gradients in the bulk for the model (4)–(8) with nonlinear bulk-surface coupling. The exact solutions are $u = v = e^t \sin(x) \sin(2y) \sin(3z)$ until final time T = 0.1 in the sphere of R = 1. The number of spherical harmonics for terms u, v and u_{rr} is 400 per each term and $v^{i+1} \approx v^i + \Delta t v_t^i$.

dynamic boundary conditions. Again, second order accuracy are observed in Tables 10 and 11 for the ∞ -, L^2 - and H^1 -norm errors. It is also interesting to notice that for this pair of exact solutions, 2-term approximation (69) and 3-term approximation (76) of the v^{i+1} term give very similar convergence results, which again illustrates the robustness of the proposed DPM-based algorithms.

In Fig. 10, we observe second order convergence of L^2 - and H^1 -norm errors both in the bulk and on the surface. Unlike the numerical results for dynamic boundary condition in



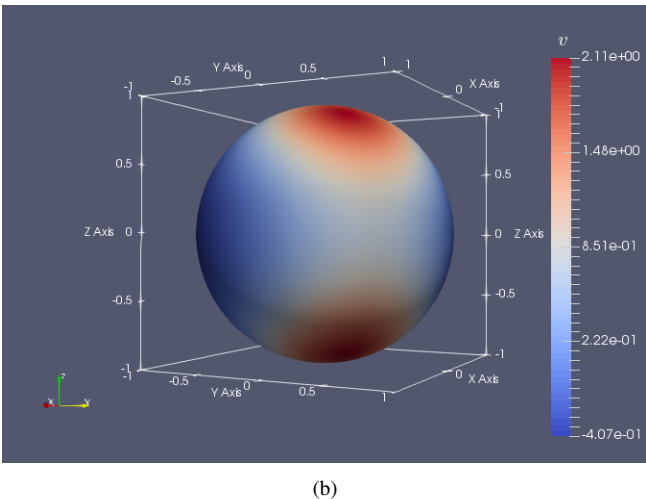


Fig. 9: 3D views of the bulk (top figure) and surface (bottom figure) approximations from mesh $255 \times 255 \times 255$ at T=0.1 to the model (4)–(8) of nonlinear bulk-surface coupling h(u,v)=uv. The exact solutions are $u=e^te^{-x(x-1)-y(y-1)}, v=e^te^{-x(x-1)-y(y-1)}(1+x(1-2x)+y(1-2y))$ in the sphere of R=1, and $v^{i+1}\approx v^i+\Delta tv^i_t+\Delta t^2v^i_{tt}/2$.

Fig. 4, the L^2 - and H^1 -norm errors in the bulk are larger than the errors on the surface in Fig. 10, which is also observed in the first test of the nonlinear coupling in Fig. 8, as well as in the test of linear bulk-surface coupling in Fig. 6.

In Fig. 11, we present the 3D views of the isosurface plots in the bulk and the plot of surface solutions, obtained on mesh $255 \times 255 \times 255$ at final time T = 0.1.

$N \times N \times N$	$E_{\infty(\Omega)}:u$	Rate	$E_{L^2(\Omega)}:u$	Rate	$E_{H^1(\Omega)}:u$	Rate
$31 \times 31 \times 31$	1.5302 E-3	_	1.0646 E-3	_	5.0709 E-3	_
$63 \times 63 \times 63$	4.1025 E-4	1.90	2.6970 E-4	1.98	1.2861 E-3	1.98
$127 \times 127 \times 127$	1.0691 E-4	1.94	6.7408 E-5	2.00	3.2158 E-4	2.00
$255 \times 255 \times 255$	2.6478 E-5	2.01	1.6839 E-5	2.00	8.0352 E-5	2.00
$N \times N \times N$	$E_{\infty(\Gamma)}: v$	Rate	$E_{L^2(\Gamma)}: v$	Rate	$E_{\boldsymbol{H}^1(\Gamma)}:v$	Rate
$31 \times 31 \times 31$	3.4599 E-5	_	4.8766 E-5	_	1.2807 E-4	_
$63 \times 63 \times 63$	9.7036 E-6	1.83	1.3621 E-5	1.84	3.5923 E-5	1.83
$127 \times 127 \times 127$	2.6424 E-6	1.88	3.6432 E-6	1.90	9.6663 E-6	1.89
$255 \times 255 \times 255$	6.7367 E-7	1.97	9.3640 E-7	1.96	2.4564 E-6	1.98
$N \times N \times N$	$E_{\infty(\Omega)}: \nabla_x u$	Rate	$E_{\infty(\Omega)}: \nabla_{\mathcal{Y}} u$	Rate	$E_{\infty(\Omega)}: \nabla_z u$	Rate
$31 \times 31 \times 31$	3.4453 E-3	_	4.6325 E-3	_	5.0779 E-3	_
$63 \times 63 \times 63$	8.8748 E-4	1.96	1.0970 E-3	2.08	1.1997 E-3	2.08
$127 \times 127 \times 127$	2.1871 E-4	2.02	2.7758 E-4	1.98	3.0294 E-4	1.99
$255 \times 255 \times 255$	5.5442 E-5	1.98	6.9999 E-5	1.99	7.5981 E-5	2.00

Table 11: Convergence of the ∞ -, L^2 - and H^1 -norm errors of the solutions in the bulk/surface, and the ∞ -norm errors of gradients in the bulk for the model (4)–(8) with nonlinear bulk-surface coupling. The exact solutions are $u = v = e^t \sin(x) \sin(2y) \sin(3z)$ until final time T = 0.1 in the sphere of R = 1. The number of spherical harmonics for terms u, v and u_{rr} is 400 per each term and $v^{i+1} \approx v^i + \Delta t v_t^i + \Delta t^2 v_{tt}^i / 2$.

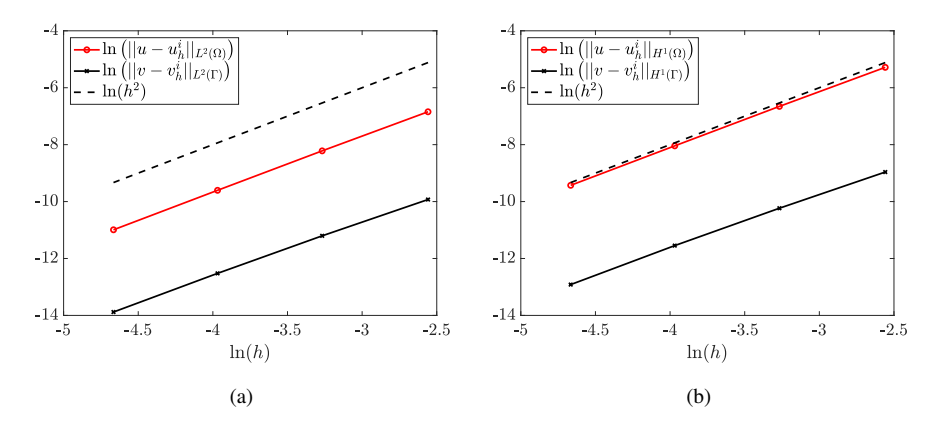
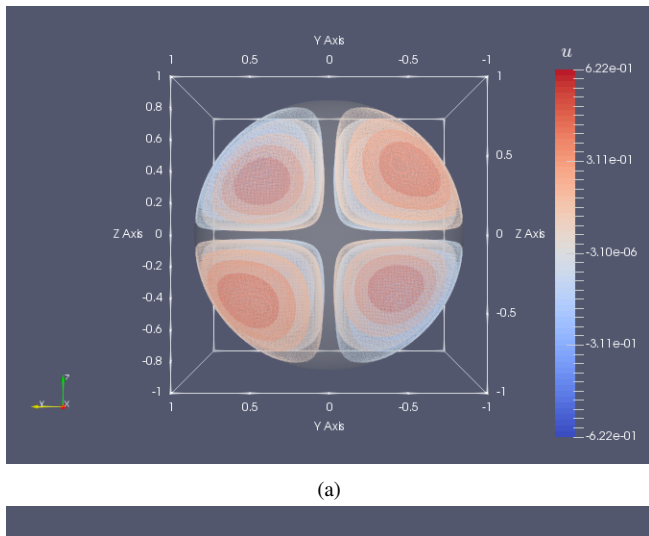


Fig. 10: Log-log plots of bulk/surface L^2 -norm errors (left figure) and bulk/surface H^1 -norm errors (right figure) for the model (4)–(8) with nonlinear bulk-surface coupling h(u,v)=uv. The exact solutions are $u=v=e^t\sin(x)\sin(2y)\sin(3z)$ until final time T=0.1 in the sphere of R=1, and $v^{i+1}\approx v^i+\Delta t v^i_t+\Delta t^2 v^i_{tt}/2$.

4.6 Condition Numbers

In Table 12, we demonstrate the condition numbers of the normal matrices from the resulting algebraic systems (77) in $Case\ 1$, (78) in $Case\ 2$: a), and (79)–(80) in $Case\ 2$: b). Note that in $Case\ 1$) and $Case\ 2$: a), the normal matrices are pre-computed outside of the time loop, while in $Case\ 2$: b), the normal matrices need to be assembled at each time step due to the nonlinearity. Thus, in Table 12, the condition numbers for $Case\ 2$: b) are computed only at the first and last time steps.



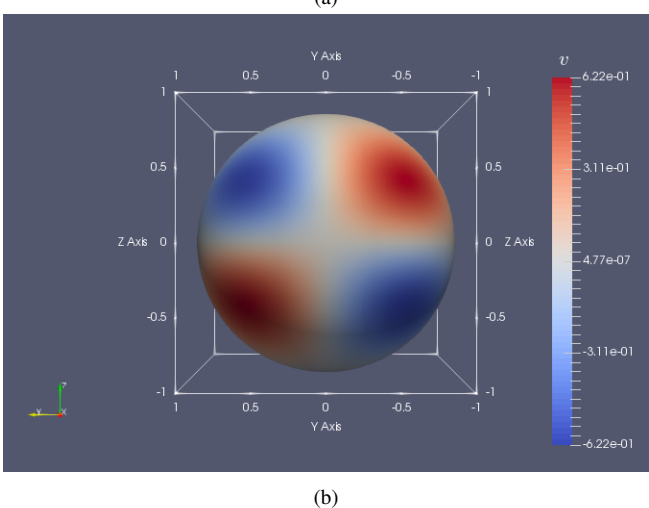


Fig. 11: 3D views of the bulk (top figure) and surface (bottom figure) approximations from mesh $255 \times 255 \times 255$ at T=0.1 to the model (4)–(8) of nonlinear bulk-surface coupling h(u,v)=uv. The exact solutions are $u=v=e^t\sin(x)\sin(2y)\sin(3z)$ in the sphere of R=1, and $v^{i+1}\approx v^i+\Delta t v_t^i+\Delta t^2 v_{tt}^i/2$.

N	Case 1 Test 2 (at $t = 0$)	Case 2:a (at $t = 0$)	Case 2:b Test 1 (w/o v_{tt} at $t = 0$)	Case 2:b Test 1 $(w/v_{tt} \text{ at } t = 0)$	Case 2:b Test 1 (w/v_{tt}) at $t = 0.1$
31	3.4838 E+1	1.7962 E+4	2.7494 E+4	2.7565 E+4	2.2402 E+4
63	4.4475 E+1	1.7659 E+3	3.7456 E+3	3.7483 E+3	3.8275 E+3
127	3.2709 E+1	3.4449 E+2	8.3878 E+2	8.3901 E+2	7.5131 E+2
255	4.0182 E+1	6.9272 E+2	9.1638 E+2	9.1639 E+2	9.0053 E+2

Table 12: Condition number of the normal matrices of BEP (notation "w/o v_{tt} " denotes 2-term approximation (69) and notation "w/ v_{tt} " denotes 3-term approximation (76)).

Furthermore, we verified that condition numbers of the normal matrices remain in similar magnitude over time for the nonlinear models in *Case 2: b*). See the last two columns in Table 12.

Acknowledgements The authors wish to thank P. Bowman and M. Cuma for assistance in computing facility, the CHPC at the University of Utah for providing computing allocations. The authors are also grateful to the referees for their most valuable suggestions. Yekaterina Epshteyn also acknowledges partial support of Simons Foundation Grant No. 415673.

References

- 1. Abramowitz, M., Stegun, I.A. (eds.): Handbook of mathematical functions with formulas, graphs, and mathematical tables. Dover Publications, Inc., New York (1992). Reprint of the 1972 edition
- Albright, J., Epshteyn, Y., Steffen, K.R.: High-order accurate difference potentials methods for parabolic problems. Appl. Numer. Math. 93, 87–106 (2015). doi:10.1016/j.apnum.2014.08.002
- Albright, J., Epshteyn, Y., Xia, Q.: High-order accurate methods based on difference potentials for 2D parabolic interface models. Commun. Math. Sci. 15(4), 985–1019 (2017). doi:10.4310/CMS.2017.v15.n4.a4
- Bardsley, P., Barmak, K., Eggeling, E., Epshteyn, Y., Kinderlehrer, D., Ta'asan, S.: Towards a gradient flow for microstructure. Atti Accad. Naz. Lincei Rend. Lincei Mat. Appl. 28(4), 777–805 (2017). doi:10.4171/RLM/785
- Barrett, J.W., Garcke, H., Nürnberg, R.: Stable finite element approximations of two-phase flow with soluble surfactant. J. Comput. Phys. 297, 530–564 (2015). doi:10.1016/j.jcp.2015.05.029
- Burman, E., Hansbo, P., Larson, M.G., Zahedi, S.: Cut finite element methods for coupled bulk–surface problems. Numerische Mathematik 133(2), 203–231 (2015). doi:10.1007/s00211-015-0744-3
- Chen, K.Y., Lai, M.C.: A conservative scheme for solving coupled surface-bulk convection-diffusion equations with an application to interfacial flows with soluble surfactant. J. Comput. Phys. 257(part A), 1–18 (2014). doi:10.1016/j.jcp.2013.10.003
- Chernyshenko, A.Y., Olshanskii, M.A.: An adaptive octree finite element method for PDEs posed on surfaces. Comput. Methods Appl. Mech. Engrg. 291, 146–172 (2015). doi:10.1016/j.cma.2015.03.025
- Chernyshenko, A.Y., Olshanskii, M.A., Vassilevski, Y.V.: A hybrid finite volume–finite element method for bulk-surface coupled problems. J. Comput. Phys. 352, 516–533 (2018). doi:10.1016/j.jcp.2017.09.064
- Coclite, G.M., Favini, A., Goldstein, G.R., Goldstein, J.A., Romanelli, S.: Continuous dependence on the boundary conditions for the Wentzell Laplacian. Semigroup Forum 77(1), 101–108 (2008). doi:10.1007/s00233-008-9068-2
- Coclite, G.M., Goldstein, G.R., Goldstein, J.A.: Stability estimates for parabolic problems with Wentzell boundary conditions. J. Differential Equations 245(9), 2595–2626 (2008). doi:10.1016/j.jde.2007.12.006
- Cusseddu, D., Edelstein-Keshet, L., Mackenzie, J., Portet, S., Madzvamuse, A.: A coupled bulk-surface model for cell polarisation. Journal of Theoretical Biology (2018). doi:10.1016/j.jtbi.2018.09.008
- 13. Dziuk, G., Elliott, C.M.: Finite element methods for surface PDEs. Acta Numer. **22**, 289–396 (2013). doi:10.1017/S0962492913000056
- Elliott, C.M., Ranner, T.: Finite element analysis for a coupled bulk-surface partial differential equation. IMA J. Numer. Anal. 33(2), 377–402 (2013). doi:10.1093/imanum/drs022
- Elliott, C.M., Ranner, T., Venkataraman, C.: Coupled bulk-surface free boundary problems arising from a mathematical model of Receptor-Ligand dynamics. SIAM Journal on Mathematical Analysis 49(1), 360–397 (2017). doi:10.1137/15m1050811
- Elliott, C.M., Ranner, T., Venkataraman, C.: Coupled bulk-surface free boundary problems arising from a mathematical model of receptor-ligand dynamics. SIAM J. Math. Anal. 49(1), 360–397 (2017). doi:10.1137/15M1050811
- 17. Epshteyn, Y.: Algorithms composition approach based on difference potentials method for parabolic problems. Commun. Math. Sci. 12(4), 723–755 (2014). doi:10.4310/CMS.2014.v12.n4.a7
- Epshteyn, Y., Xia, Q.: Efficient numerical algorithms based on difference potentials for chemotaxis systems in 3D. J. Sci. Comput. 80(1), 26–59 (2019). doi:10.1007/s10915-019-00928-z
- Gross, S., Olshanskii, M.A., Reusken, A.: A trace finite element method for a class of coupled bulk-interface transport problems. ESAIM Math. Model. Numer. Anal. 49(5), 1303–1330 (2015). doi:10.1051/m2an/2015013

- Hansbo, P., Larson, M.G., Zahedi, S.: A cut finite element method for coupled bulk-surface problems on time-dependent domains. Computer Methods in Applied Mechanics and Engineering 307, 96–116 (2016). doi:10.1016/j.cma.2016.04.012
- 21. Kovács, B., Lubich, C.: Numerical analysis of parabolic problems with dynamic boundary conditions. IMA Journal of Numerical Analysis 37(1), 1–39 (2016). doi:10.1093/imanum/drw015
- 22. Liu, C., Wu, H.: An energetic variational approach for the cahn-hilliard equation with dynamic boundary conditions: Derivation and analysis. Archive for Rational Mechanics and Analysis (2019)
- 23. Ludvigsson, G., Steffen, K.R., Sticko, S., Wang, S., Xia, Q., Epshteyn, Y., Kreiss, G.: High-Order Numerical Methods for 2D Parabolic Problems in Single and Composite Domains. J. Sci. Comput. **76**(2), 812–847 (2018). doi:10.1007/s10915-017-0637-y
- Madzvamuse, A., Chung, A.H.: The bulk-surface finite element method for reaction-diffusion systems on stationary volumes. Finite Elements in Analysis and Design 108, 9 21 (2016). doi:https://doi.org/10.1016/j.finel.2015.09.002
- 25. Magura, S., Petropavlovsky, S., Tsynkov, S., Turkel, E.: High-order numerical solution of the Helmholtz equation for domains with reentrant corners. Appl. Numer. Math. 118, 87–116 (2017). doi:10.1016/j.apnum.2017.02.013
- Massing, A.: A cut discontinuous galerkin method for coupled bulk-surface problems. In: S.P.A. Bordas,
 E. Burman, M.G. Larson, M.A. Olshanskii (eds.) Geometrically Unfitted Finite Element Methods and Applications, pp. 259–279. Springer International Publishing, Cham (2017)
- Medvinsky, M., Tsynkov, S., Turkel, E.: Direct implementation of high order BGT artificial boundary conditions. J. Comput. Phys. 376, 98–128 (2019). doi:10.1016/j.jcp.2018.09.040
- 28. Novak, I.L., Gao, F., Choi, Y.S., Resasco, D., Schaff, J.C., Slepchenko, B.M.: Diffusion on a curved surface coupled to diffusion in the volume: Application to cell biology. Journal of Computational Physics **226**(2), 1271–1290 (2007). doi:10.1016/j.jcp.2007.05.025
- Olshanskii, M.A., Reusken, A.: A finite element method for surface PDEs: matrix properties. Numer. Math. 114(3), 491–520 (2010). doi:10.1007/s00211-009-0260-4
- Olshanskii, M.A., Reusken, A.: Trace finite element methods for PDEs on surfaces. In: Geometrically unfitted finite element methods and applications, *Lect. Notes Comput. Sci. Eng.*, vol. 121, pp. 211–258.
 Springer, Cham (2017)
- 31. Petropavlovsky, S., Tsynkov, S., Turkel, E.: A method of boundary equations for unsteady hyperbolic problems in 3D. J. Comput. Phys. 365, 294–323 (2018). doi:10.1016/j.jcp.2018.03.039
- Ryaben'kii, V.S.: Method of difference potentials and its applications, Springer Series in Computational Mathematics, vol. 30. Springer-Verlag, Berlin (2002). doi:10.1007/978-3-642-56344-7. Translated from the 2001 Russian original by Nikolai K. Kulman.
- 33. Ryaben'kii, V.S., Turchaninov, V.I., Epshteyn, Y.Y.: Algorithm composition scheme for problems in composite domains based on the difference potential method. Computational Mathematics and Mathematical Physics 46(10), 1768–1784 (2006). doi:10.1134/s0965542506100137
- 34. Vázquez, J.L., Vitillaro, E.: Heat equation with dynamical boundary conditions of reactive–diffusive type. Journal of Differential Equations 250(4), 2143–2161 (2011). doi:10.1016/j.jde.2010.12.012